IAEA nuclear fusion

PAPER • OPEN ACCESS

An extensive analysis of SOL properties in high-δ plasmas in ASDEX Upgrade

OPEN ACCESS
IOP Publishing | International Atomic Energy Agency

Nuclear Fusion

Nucl. Fusion **64** (2024) 086064 (21pp)

https://doi.org/10.1088/1741-4326/ad5457

An extensive analysis of SOL properties in high-δ plasmas in ASDEX Upgrade

A. Redl[1,*], T. Eich[2,3], N. Vianello[4,5], J. Adamek[6], M. Bernert[2], G. Birkenmeier[2], D. Brida[2], P. David[2], M. Faitsch[2], R. Fischer[2], G. Grenfell[2], R. Ochoukov[2], V. Rohde[2], B. Tal[2], M. Dreval[7], the ASDEX Upgrade Team[a] and the EUROfusion Tokamak Exploitation Team[b]

[1] DEIM Department, Universitá degli Studi della Tuscia, Campus Riello, Blocco F, 01100 Viterbo, Italy
[2] Max Planck Institute for Plasma Physics, Boltzmannstr. 2, 85748 Garching, Germany
[3] Commonwealth Fusion Systems, 111 Hospital Rd, Devens, MA 01434, United States of America
[4] Consorzio RFX (CNR, ENEA, INFN, Universitá di Padova, Acciaierie Venete SpA), Corso Stati Uniti 4, 35127 Padova, Italy
[5] Istituto per la Scienza e la Tecnologia dei Plasmi, CNR, 35127 Padova, Italy
[6] Institute of Plasma Physics of the CAS, Za Slovankou 1782/3, 182 00 Praha 8, Czech Republic
[7] Institute of Plasma Physics, National Science Center, Kharkov Institute of Physics and Technology, 61108 Kharkov, Ukraine

E-mail: Andreas.Redl@unitus.it

Received 7 December 2023, revised 13 May 2024
Accepted for publication 5 June 2024
Published 15 July 2024

Abstract

A set of dedicated H-mode discharges with constant heating power combining Neutral Beam Injection and Electron Cyclotron Resonance Heating have been executed at the ASDEX Upgrade tokamak using a high triangularity magnetic geometry in order to investigate the impact of filamentary transport to divertor and non-divertor components. The evolution of upstream scrape-off layer (SOL) profiles have been correlated with dedicated separatrix quantities, mostly with the turbulence control parameter α_t (Eich and Manz 2021 *Nucl. Fusion* **61** 086016) describing the turbulence level at the separatrix. With increasing α_t, a broadening of the upstream density profiles in the near-SOL together with the formation of a density shoulder in the far-SOL have been observed. This phenomenon is associated with an enhanced filamentary transport dominating the radial turbulent transport in the far-SOL and confirmed by means of the cooling water calorimetry on non-divertor components. The probe measurements conducted with the ball-pen probe-head mounted on the midplane manipulator and a retarding-field analyzer close to the limiter surface indicate that the key mechanism increasing the radial filamentary transport to the first wall is an increase of the particle flux $\Gamma_{r,fil}$, caused primarily by the packing fraction $f_{PF,fil}$ and the filament density $n_{e,fil}$. At the same time, the electron temperature T_e and ion temperature T_i measured close to the limiter surface show only

[a] See Zohm *et al* 2024 (https://doi.org/10.1088/1741-4326/ad249d) for the ASDEX Upgrade Team.
[b] See Joffrin *et al* 2024 (https://doi.org/10.1088/1741-4326/ad2be4) for the EUROfusion Tokamak Exploitation Team.
[*] Author to whom any correspondence should be addressed.

small variations above $\alpha_t > 0.5$. Both the filamentary heat flux and the gross erosion derived from the first wall probe measurements reach a magnitude that should be considered in the design of future fusion reactors.

Keywords: ASDEX Upgrade, power exhaust, QCE regime, filamentary transport

(Some figures may appear in colour only in the online journal)

1. Introduction

The proper understanding of the physical mechanism driving the convective transport in the scrape-off layer (SOL) region is of utmost importance for the extrapolation to future fusion power plants. The heat load handling capability of the plasma-facing components (PFCs) of both, the divertor plates and of the first wall, is limited by engineering constraints in order to avoid material fatigue (tungsten recrystallization, melting and/or excessive erosion, ...).

Due to these engineering constraints, several scenarios which attempt to handle the power exhaust challenge by exploiting different approaches are under intensive investigations. One of those candidates is the so-called '*Quasi-Continuous-Exhaust*' (QCE) regime [1]. This scenario combines high plasma core density $n_{\mathrm{e,core}}$ (close to 1.0 n_{GW} [2]) and high separatrix density $n_{\mathrm{e,sep}}$ (up to 0.7 n_{GW} reached as well with pellet fuelling [3]) at high upper triangularity δ_{u}, close to double-null (CDN) shaping. Beside the relevance of high $n_{\mathrm{e,sep}}$ in order to achieve both, high volumetric radiation losses in the SOL [4] and high neutral recycling state and divertor detachment [5], high separatrix density plays a key role in the mechanism according to which [6–10] Type-I edge-localized modes (ELMs) [11, 12] are replaced by small, high frequently, incoherent filamentary bursts [13, 14]. As known from previous work in AUG at high $n_{\mathrm{e,sep}}$ [15], a broadening of the *e*-folding temperature and density decay lengths λ_{t} and λ_{n} is also observed in the QCE regime together with the formation of a density shoulder which is associated with an enhancement of filamentary activities in the far-SOL [1, 14, 16–20].

Over the last years, a novel theoretical framework has been developed [21, 22] attempting to describe properly the widening of the SOL decay lengths by a set of dimensionless parameters assessing the turbulence level by separatrix conditions. This model is based on the Drift-Alfven (DALF) turbulence model and linked to pioneering studies introduced in [23–25]. Within this framework, a novel parameter, the so-called turbulence control parameter α_{t} is introduced. This parameter, which describes the relative strength of drift vs interchange turbulent fluctuations around the separatrix, can be expressed for AUG conditions according to [21, 22] as:

$$\alpha_{\mathrm{t}} \approx 3.0 \cdot 10^{-18} R \hat{q}_{\mathrm{cyl}}^2 \frac{n_{\mathrm{e,sep}}}{T_{\mathrm{e,sep}}^2} Z_{\mathrm{eff}}, \qquad (1)$$

where R denotes the geometric major radius, $\hat{q}_{\mathrm{cyl}}$ the cylindrical safety factor, $T_{\mathrm{e,sep}}$ the separatrix electron temperature and Z_{eff} the effective charge number.

The QCE scenario combines features interesting for ITER or future fusion reactors. However, to date, the full extent of the enhanced filamentary transport is not yet known, which may lead to new challenges for the PFC material of non-divertor components, in particular for the first wall PFCs [26–28]. Until now, an in-depth analysis of the consequences of the convective transport with respect to the power exhaust of H-mode discharges is still missing.

The study presented in this manuscript reports on the assessment of the SOL transport combining non-calorimetric and calorimetric measurements and attempts to connect the evolution of upstream separatrix and SOL properties to changes of downstream SOL profiles and of PFC energy load distributions. Furthermore, the impact of the upstream SOL profiles on the density shoulder amplitude are assessed considering also neutral pressure and neutral flux measurements in the main chamber and in the divertor. Using dedicated probe measurements at the midplane level, the key mechanism behind the enhancement of filamentary transport is investigated and its heat flux is compared to the calorimetrically estimated heat flux. Probe measurements also allows to estimate the gross erosion which is of interest for the ITER first wall.

The paper is structured as followed: in section 2, diagnostics are briefly introduced. Due to the use of calorimetric diagnostics, certain boundaries in the discharge configuration are required leading to a dedicated database, which are shortly discussed. In section 3, first results shown in [29] are extended to any PFCs of AUG and discussed more detailed. In the subsequent section 4, the upstream and downstream profiles are discussed and correlated with upstream separatrix conditions. In section 5, the probe measurements conducted close to the limiter surface are assessed in order to identify the key quantities associated with the increased filamentary activities. A power balance comparing probe with calorimetric results is presented. A simple estimation of the gross erosion to be expected on non-divertor PFCs based on probe measurements is also provided. The section 6 summarizes this study.

2. Experimental setup for the characterization of the filamentary energy transport in high-density high-δ H-mode discharges in AUG

2.1. An overview of non-calorimetric diagnostics to assess the consequences of convective transport in the SOL

To measure and quantify properly the consequences of the turbulent activities at the separatrix in the near- and far-SOL, a set of dedicated diagnostics covering areas both around the midplane and close to the divertor target. When it is not explicitly mentioned, all parameters in this study are averaged over

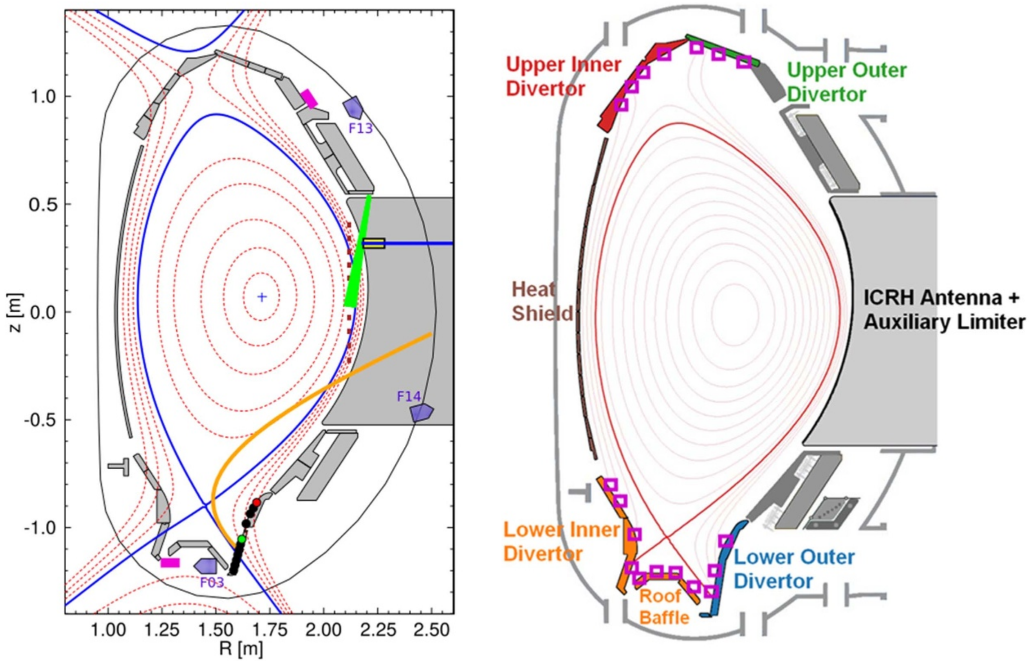

Figure 1. Left: poloidal cross section of AUG illustrating the set of diagnostics and their spatial coverage. The LOS of the IR thermography focused on the main target is indicated as orange line, the LOS of the edge TS diagnostic as brown squares, the LOS distribution of the CXRS as green lines and the spatial distribution of the LP at the main target as black dots. The red marker denotes top LP of Tile 1 and the red marker the top LP of Tile 2. The poloidal position of the MEM equipped with the BPP-head (blue), the RFA2 (yellow with black contour), the entrance of the baratron close to the upper divertor and the below the roof baffle (purple markers) and the three manometers (dark blue markers) are added. The LOS of the LIB is at the same poloidal position as the MEM and therefore not shown. The plot also illustrates the high-δ magnetic equilibrium used in this study. Right: poloidal cross section of AUG indicating the coverage of the cooling units (colour highlighted areas and labels) available through the revised cooling water calorimetry. Each purple marker indicates one thermocouple providing an additional high-spatial poloidal coverage of the lower/upper divertor in single segments of AUG. Reproduced from [35].

the time interval 3.0–7.0 s. Figure 1(left) provides an overview of the involved non-calorimetric diagnostics, whereas figure 1(right) provides a distribution of calorimetric diagnostics. The orange line illustrates the line of sight (LOS) of the infrared (IR)-thermography [30] with focus on the outer divertor target. The IR-thermography measures the tile surface temperature, which is used as input for the implicit version [31] of THEODOR [32]. Applying the Eich-fit [33] allows to determine λ_q and the divertor broadening S from the heat flux density profile. λ_q and S are remapped to the outer midplane (OMP) by exploiting the appropriate flux expansion f_x [34].

The black dots indicate the position of Langmuir probes (LPs) installed in the lower outer divertor. At AUG, so-called *'triple'* probes are used allowing a robust and simple evaluation [36] of the downstream profiles of the ion saturation current density j_{sat}, the electron density n_{e}, the electron temperature T_{e} and the perpendicular heat flux $q_{\perp}$.

The baratrons [37, 38] measuring the neutral pressure p_{n} close to the upper and in the divertor are also taken into account. The upper divertor entrance (purple rectangle) is located between the upper outer divertor and the passive stabilization loop (PSL, [39]) at the low field side, whereas the divertor entrance (purple rectangle) is located in the roof baffle close to the inner divertor. p_{n} is seen as an engineering parameter which depends on the fuelling level and the pumping speed. The measurements are calibrated to represent the neutral pressure at the port entrance and is a proxy for the neutral fluxes. Additionally, AUG is equipped with several manometers [40] at different poloidal and toroidal positions in order to measure the neutral flux density. The ones used in this study are indicated in figure 1(left) as dark blue markers. F03 denotes a manometer operating in the roof baffle, F13 a manometer operating close to the upper divertor comparable to the upper divertor baratron. F14 operates in the LFS main chamber in the open region below the midplane.

To obtain $n_{\mathrm{e,sep}}$ [in $1\,\mathrm{m}^{-3}$] and $T_{\mathrm{e,sep}}$ [in eV] and their respective *e*-folding decay lengths in the near-SOL, the edge TS diagnostic (brown squares) [41] is utilized. To determine accurately and robustly the values at the separatrix (challenging due to the presence of steep gradients between pedestal and separatrix), a power balance approach is applied assuming the *'Spitzer-Härm'* electron heat conduction being the dominant transport around the separatrix [42]. This approach yields an expression for $T_{\mathrm{e,sep}}$:

$$T_{\mathrm{e,sep}} \approx \left(\frac{7 P_{\mathrm{sep}} q_{\mathrm{cyl}}^2 R}{16 \kappa_0 \hat{\kappa} a \langle \lambda_{\mathrm{q}} \rangle}\right)^{\frac{2}{7}}, \tag{2}$$

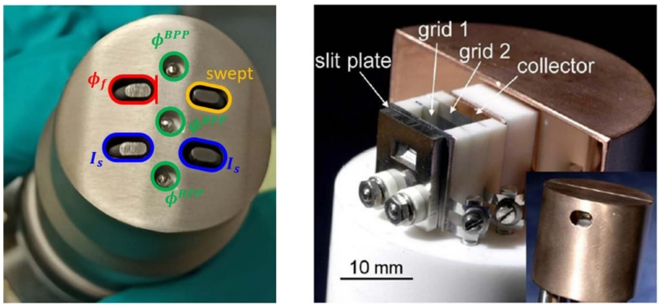

Figure 2. Left: tip of the BPP head visualizing a possible probe configuration of the 3 BPPs (green indicated) and the 4 LPs (blue, red and yellow indicated). Reproduced from [47]. Right: Close-Up of the tip of the RFA2 probe head showing the slit plate, grids, and collector. The plot in the right corner shows the RFA2 head with its full graphite housing. Reproduced from [48].

where P_{sep} [in W] denotes the power crossing the separatrix, a the minor radius, κ_0 the Spitzer-Härm thermal heat conductivity, $\langle\lambda_q\rangle$ the poloidally averaged power width in the near-SOL taken and $\hat{\kappa}$ is defined as [21]:

$$\hat{\kappa} = \sqrt{\frac{1+\kappa^2\left(1+2\delta^2-1.2\delta^3\right)}{2}}. \quad (3)$$

An iterative numerical scheme solves equation (2) searching for $T_{e,sep}$ in the TS electron temperature profiles, where the calculated and the measured $T_{e,sep}$ matches within 2%. The identified $T_{e,sep}$ corresponds to $\rho_{pol} = 0.999$.

The Lithium-beam emission spectroscopy (LIB) [43] is considered to measure the evolution of the density in the near- and far-SOL in order to qualify the density shoulder amplitude. Its LOS overlaps with the LOS of the midplane manipulator (MEM) (blue line in figure 1 (left)).

For an in-depth analysis of filamentary turbulence, which is considered as the most likel candidate to explain the modifications in the transport in the far SOL, probe measurements were performed in all discharges consisting of the retarding field analyzer (RFA2) [44] to determine the ion temperature T_i and the ball-pen probe (BPP)-head [45–47] to determine quantities describing the filament characteristics. The demanded quantities are briefly introduced in the subsequent paragraph. The BPP-head was mounted on the MEM. Both probe-heads operate at the same poloidal position, which is about 35 cm above the midplane, but at different toroidal positions. They were plunged several times in each discharge and each plunge lasted about 200 ms. The measurements of both probe heads were taken about 1 cm in front of the limiter to ensure a safe operation for both the diagnostics and for the overall plasma.

To determine all relevant quantities in order to assess the radial convective transport, the BPP-head is equipped with 3 BPP pins and 4 LPs. The configuration of the spatial probe distribution as used in this study is shown in figure 2. The 3 probes indicated in green are the BPPs on floating configuration ϕ^{BPP}, the blue indicated LPs measuring the ion saturation current I_{sat}, the red LP the floating potential ϕ_f and the orange one labelled *'swept'* the electron temperature T_e, j_{sat} and ϕ_f.

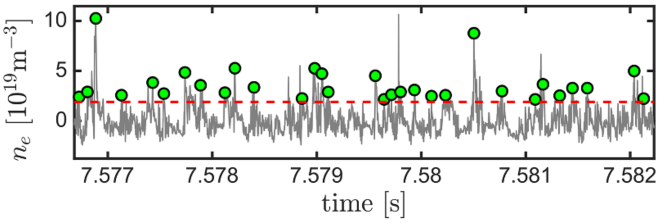

Figure 3. Timetrace of the density of a single plunge to illustrate the signal peaks as detection criterion. The horizontal red dashed line represents the threshold criterion according to equation (4). The green markers indicate the peaks which are identified as filaments.

The offset of each signal is subtracted by a running median filter. The BPP-head operates with an acquisition frequency of 2 MHz. The detection of filaments follows mostly commonly accepted approaches [47, 49, 50]. The analysis shown here uses a modified threshold criterion in the density amplitude. The fundamental criterion being detected as filament is defined as:

$$I_{sat}^{pk} > 1.5\sigma + \langle I_{sat}\rangle, \quad (4)$$

where I_{sat}^{pk} denotes the amplitude peak, σ the standard deviation and $\langle I_{sat}\rangle$ the mean value of the time interval chosen for the evaluation. Not all peaks above the threshold criterion are identified as filaments. Next to the threshold criterion (equation (4)), a filament must additionally fulfill a minimum peak width ($\omega_{sat}^{pk} = 5\mu s$), a peak distance ($d_{sat}^{pk} = 100\,\mu s$) and a correlation criterion introduced in [51]. In figure 3, the red dashed horizontal line denotes the threshold criterion as defined in equation (4) and the green markers denote peaks detected to be filaments.

The criterion to decide what a filament is is somehow arbitrary, as it can always be modified or even improved (when you have more prior information). In fact, different criteria have been used in the literature, which is detailed reported in [50]. Here, we used a simple threshold criterion, where filaments are defined as the peaks in density fluctuation above this threshold. In addition, criteria defined for their time duration (to exclude peaks that are not from coherent structures), the time between events (which is set longer than the filament correlation time to avoid counting a filament twice), and the correlation between the peaks (to ensure they have a similar shape) are taken into account. The peaks with too short time width are typically not coherent structures, so they are disregarded as filaments (although they can still induce transport). We have not seen great differences when changing the threshold, particularly in the transport evaluation. For example, when the threshold is set larger than what we used, the mean density of filaments becomes larger, but the number of detected filaments decreases. As the mean filament correlation time is not much modified, the packing fraction decreases, which compensates for the increase in density, leading to roughly the same level of transport. In short, we acknowledge that the criterion to define filament is arbitrary, but the paper's general conclusions are not modified if we use a different criterion.

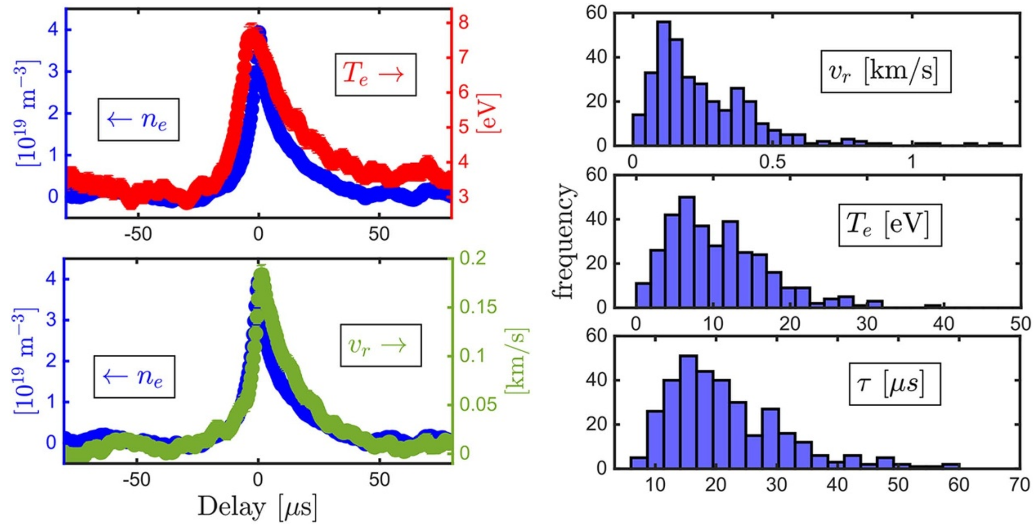

Figure 4. Left: identified peaks and the derived quantities filament density n_e, filament radial velocity v_r and filament electron temperature T_e following the condition in equation (4) and conditional averaged. Right: histogram distribution of v_r, T_e and the filament correlation time τ of all detected filaments of a single plunge.

For each identified filament, several quantities can be derived. Figure 4(left) illustrates the density n_e, radial velocity v_r and electron temperature T_e derived from conditional average sampling utilizing the identified peaks in ion saturation current associated with filaments. T_e can be derived from:

$$T_e = \frac{\phi^{BPP} - \phi_f}{\alpha^{LP} - \alpha^{BPP}}, \tag{5}$$

where α^{LP} and α^{BPP} denote the LP and BPP coefficients [47], For α^{LP}, an analytical formula is given [42], whereas for α^{BPP} it must be experimentally determined [47]. The quantity v_r, which is caused by the *E*x*B*-drift of filaments [49], can be expressed by:

$$v_r = \frac{\Delta\phi^{BPP}}{d \cdot B}, \tag{6}$$

where $\Delta\phi^{BPP}$ denotes the potential fluctuation difference between two BPP, d the poloidally displaced distance between these two BPPs and B the magnetic field strength at the tip. As the LPs acts as a mach probe, the parallel Mach number $M_\parallel$ [52] is approximated by the expression:

$$M_\parallel = \frac{v_\parallel}{c_s} \approx 0.44 \log\left(\frac{j_{sat,up}}{j_{sat,down}}\right), \tag{7}$$

where $j_{sat,i}$ denotes I_{sat} of the respective LP divided by the probe surface area A. n_e determined from a Mach probe can be expressed by:

$$n_e \approx \frac{1}{2ec_s}\left(\frac{j_{sat,up}}{\gamma^{up}} + \frac{j_{sat,down}}{\gamma^{down}}\right), \tag{8}$$

where $c_s \approx \sqrt{(T_i + T_e)/m_i}$ denotes the sound speed, e the electric charge and γ^{down} is defined as [52]:

$$\gamma^{down}\left(M_\parallel\right) = e^{\left(-1-1.1\cdot M_\parallel\right)}. \tag{9}$$

Based on that, γ^{up} is defined as:

$$\gamma^{up}\left(M_\parallel\right) = \gamma^{down}\left(-M_\parallel\right). \tag{10}$$

The filament correlation time τ is based on the double *'Full Width at Half Maximum (FWHM)'* of an exponential decay function fitted to the peak profile. Multiplying τ with the filament detection frequency ν_{detect}, which describes the number of detected filaments within a certain time interval, provides the so-called packing fraction f_{PF} [53]. As last quantity, one can define the particle flux Γ_r which is defined as:

$$\Gamma_r = f_{PF} n_e v_r. \tag{11}$$

For each plunge, all detected filaments are collected in order to derive the quantities as introduced above. For each quantity and plunge a histogram distribution can be provided. The filamentary quantities are obtained from their respective distributions. The background quantities are defined as the mean value of each plunge.

The setup of the RFA2 probe-head follows common designs [54, 55]. The RFA2 exploits a novel probabilistic approach in order to determine T_i. A detailed description of the full probabilistic approach is provided in [44]. In the presented study, the RFA2 sweeps its current–voltage characteristics with 5 kHz. The choice of 5 kHz is a compromise due to the use of NBI and short plunge durations. The probability distribution functions (PDF) obtained for both grids (side A and B) are illustrated in figure 5. The PDFs of both grids are averaged (firstly side *A* and *B* of each plunge and then the plunges of a single discharge) and issues the T_i-representation. Due to its field-alignment, the RFA2 actually provides $T_{i,\parallel}$ and not $T_{i,\perp}$. Because of the large distance from the separatrix, it is reasonable to assume that all degrees of freedom of the T_i-distribution are distributed equally. Therefore, it is reasonable to assume that $T_{i,\perp} = T_{i,\parallel}$, which is in agreement to previous high-density L-modes studies conducted in AUG [53]. Due to

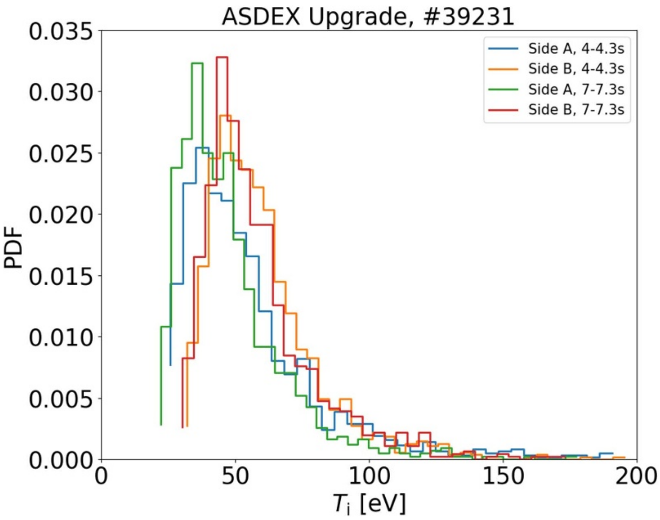

Figure 5. PDF of T_i measured close to the limiter surface by using the RFA2. Two plunges were performed lasting roughly 200 ms. Side *A* and *B* denotes the two grids as shown in figure 2(right). For each plunge, the average of side A and B is taken and afterwards the mean value of both plunges is taken for further processing.

choice of the 5 KHz sweeping frequency, the most probable T_i values are similar to commonly accepted conditional averaged values and do not resolve filamentary T_i. Even though the provided T_i-distributions do not fully catch the fluctuations usually associated with filaments, they can be considered as a lower limit for $T_{i,fil}$. Moreover, the evolution of T_i throughout the database still allows us to draw important conclusions.

The ion temperature at the separatrix $T_{i,sep}$ can be seen as upper limit for $T_{i,fil}$. In all discharges, the Charge-Exchange-Recombination-Spectroscopy (CXRS) [56, 57] (distribution of LOS indicated as green lines in figure 1(left)) has been considered in order to estimate $T_{i,sep}$. The provided T_i-profiles from the different (poloidal/toroidal) CXRS diagnostics serve as input for the *'Integrated Data Analysis for Ion profiles'* (IDI) [58] exploiting a bayesian probabilistic approach to determine the most likely profile at the separatrix.

2.2. Calorimetric diagnostics available at AUG

To measure the energy loads on all PCFs, two calorimetric diagnostics have recently become available [35, 59] and are briefly introduced here. The cooling water calorimetry (KWK) exploits the extensive cooling system of the AUG tokamak, which encompasses the entire machine and provides an almost perfect coverage of all in-vessel components. To evaluate the energy deposition, certain areas are cumulated into so-called 'cooling units' and are the smallest spatial units to resolve energy loads. The setup allows to resolve the heat shield, upper inner/outer divertor and the lower inner/outer divertor in all 16 segments separately. These cooling units are indicated as colored highlighted areas and labels in figure 1(right). To calculate the captured energy load per cooling unit Q, the formula as given in [60] has to be solved:

$$Q = m \int_{t_1}^{t_2} \Delta T c_p \mathrm{d}t, \tag{12}$$

where m denotes the flow rate of a cooling unit, ΔT the relative rise obtained from the difference of the inlet and outlet cooling water temperature, c_p is the heat capacity of the cooling water and the time interval $[t_1, t_2]$ must cover the full excursion of the relative temperature profile ΔT.

The extensive wall thermometry of AUG [60] provides tile-resolved calorimetric measurements. This system exploits 94 thermocouples covering poloidally important in-vessel components, mainly the lower (segments 4, 8, 10 and 13) and upper (segments 4 and 13) divertor. Its distribution can be found in figure 1(right). Each purple marker indicates one thermocouple. The evaluation scheme follows the approach introduced in [61], but adjusted for the AUG boundaries. This approach allows to calculate the energy stored in the tile following the formula:

$$Q = m_{\mathrm{tile}} \int_{T_{\mathrm{begin}}}^{T_{\mathrm{end}}} c_p(T)\, \mathrm{d}T, \tag{13}$$

where m_{tile} is the mass of the tile, c_p(T) is the temperature-dependent heat capacity and the boundaries (T_{end}, T_{begin}) of the integral defines the temperature rise. Fit formulae for the temperature-dependent heat capacities are taken from [62, 63].

The duration of an AUG discharge is limited to 10 s, which allows only measurements of the temperature signals during the cooling-down phase. Consequently, only time-integrated values can be provided.

2.3. Experimental setup of the highly-shaped discharge database

In order to cope with the aforementioned diagnostic constraints, including the capability of the calorimetric diagnostic to provide only time-integrated information, an appropriate shot plan has been conceived where the flat-top phase of each discharge is kept constant during the execution. Figure 1 provides an overview of the discharge configuration for reference discharge #39231 at $B_{\mathrm{tor}} = -2.45$ T. In order to identify a robust scaling parameter, the safety factor q has been varied by changing B_{tor}, whereas the plasma current I_p is kept identical at 0.8 MA in each discharge. For the database, discharges have been executed at three different B_{tor}-values: -2.45 T, -1.8 T and -2.8 T. Due to different B_{tor}-values, different heating schemes have to be used. In figure 1, panel (*b*) shows the time traces of the heating scheme combining neutral beam injection (NBI, black) and electron cyclotron resonance heating (ECRH, green). Two NBI sources and 4 ECRH gyrotrons in X2-mode providing appropriate central heating are utilized. For $B_{\mathrm{tor}} = -2.8$ T, the ECRH contribution is replaced by one additional NBI source, whereas for $B_{\mathrm{tor}} = -1.8$ T, the ECRH contribution is used in X3-mode and using 3 gyrotrons instead of 4. Radiative losses P_{rad} (red) are calculated by a novel bolometric method [64]. For the entire database, the same magnetic equilibrium with high upper triangularity δ_u (≈ 0.28) and high

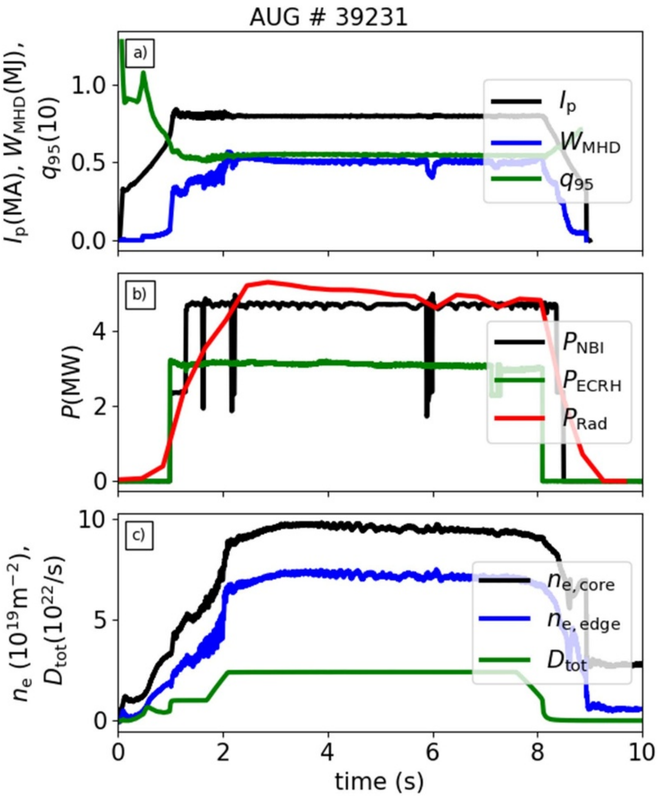

Figure 6. Experimental time traces of dedicated plasma parameters characterizing AUG discharge #39231. Panel (*a*) illustrates the plasma current I_p (black), W_{MHD} (blue) and q_{95} (green). In panel (*b*), the heating scheme combining NBI (black) and ECRH (green) in X2-mode at $B_{tor} = -2.45$ T and using 4 gyrotrons is shown. Radiative losses P_{rad} (red) are calculated by using the novel method BPT [64]. In panel (*c*), the line-integrated density of core (black) and edge (blue) acquired by the interferometer [65] is shown. The total fuelling rate D_{tot} in feed-forward is also added. All discharges are divertor-fuelled.

elongation κ (≈ 1.7), leading to a CDN shaping, is used. The shape is visualized in figure 1(left).

In order to cover a large range of the density operational space, the feed-forward fuelling level iin the flattop phase has been varied on a shot-to-shot basis. All discharges are fuelled from the divertor. Panel (*c*) in figure 6 shows the fuelling level in the flattop phase for #39231 at 2.5×10^{-22} s^{-1}. The database for this configuration cover a flat-top fuelling between 0.1×10^{-22} s^{-1} and 2.85×10^{-22} s^{-1}. The highest fuelling level was limited by the ECRH cut-off density. At $B_{tor} = -2.8$ T, the flattop fuelling covers the range between 1.75×10^{-22} s^{-1} and 3.2×10^{-22} s^{-1} and at B_{tor} = -1.8 T the range between 1.0×10^{-22} s^{-1} and 3.2×10^{-22} s^{-1}. Where the range of different B_{tor}-values overlap each other, the same flattop fuelling levels have been used. For PFC energy distribution studies, only discharges which ended without the use of killergas are considered. The use of killergas would falsify the energy distribution. The database consists of 8 discharges conducted at $B_{tor} = -2.45$ T (+2 fuelling scans to acquire missing first wall probe measurements), 5 discharges conducted at B_{tor} $= -1.8$ T and 4 discharges conducted at $B_{tor} = -2.8$ T.

3. The distribution of energy loads on AUG in-vessel components

3.1. Evolution of the PFC heat loads at dedicated areas

This section represents an extension of the energy load scaling presented in [29]. The energy balance of the database introduced in the prervious chapter is based in the results summarized in [35] and have already been reported in [29]. Here, the first wall, the lower divertor (inner and outer divertor together), the upper divertor (inner and outer divertor together) and the heat shield are separately considered and discussed.

To infer the evolution on the PFC energy loads whenever the plasma scenario moves from Type-I ELMy regimes to high density QCE regimes, all available cooling units of the AUG cooling water calorimetry are considered and arranged to represent dedicated areas. Following the notation in [66] and firstly reused in [29], the first wall in AUG is defined by the four ICRH antennas and the four auxiliary limiters (black highlighted areas and labels in figure 1(right)). The latter PFCs are installed on both sides (left and right) of each NBI duct. Following the observations in [66], ELMs can reach the auxiliary limiters and demand the consideration of these PFCs. Each ICRH antenna and auxiliary limiter acts as a single cooling unit. These 8 cooling units define the AUG first wall. The cooling units of the inner and outer divertor of AUG (orange/blue highlighted areas and labels in figure 1(right)) are in sum 32 cooling units and define the lower divertor. The 'upper divertor' follows this scheme and combines the inner and outer divertor of AUG (red/green highlighted areas and labels in figure 1(right)) which are in sum 32 cooling units. The 'heat shield' is based on the cooling units highlighted in brown in figure 1(right). This area consists of 16 cooling units.

In recent years, it has been shown at AUG experimentally [3, 6] and theoretically suggested [21, 67, 68] that the region around the separatrix emerges as a key region to describe the entire plasma performance and to characterize also the heat fluxes reaching the PFCs. As shown in figure 7(left top) the first wall energy load normalized to total energy increases almost linearly with the turbulence control parameter α_t ($\approx \nu_e^* \cdot q_{cyl}/100$). The first wall energy loads cover the, so far known, range for H-modes in α_t. The transition from QCE discharges at high fuelling to Type-I ELMy H-modes with continuously decreased flattop fuelling is gradual which is consistent with the gradual λ_q-evolution and the co-existance of Type-I ELMs with smallish filamentary ELMs as reported in [1].

Furthermore, the results for the first wall energy loads of a previous AUG study [66] is added as dashed horizontal line. At that time, 5% of the energy have been found at the first wall of a low density ELMy H-mode with carbon walls in AUG and seems to be in good agreement with latest calorimetric observations in a full-tungsten device. Separatrix values are not available due to the data quality of the edge TS at that time together with the lack of a reasonable Z_{eff}-estimate at the separatrix at AUG, which is particularly important for carbon devices. Additionally, the regression formula with respect to α_t is added.

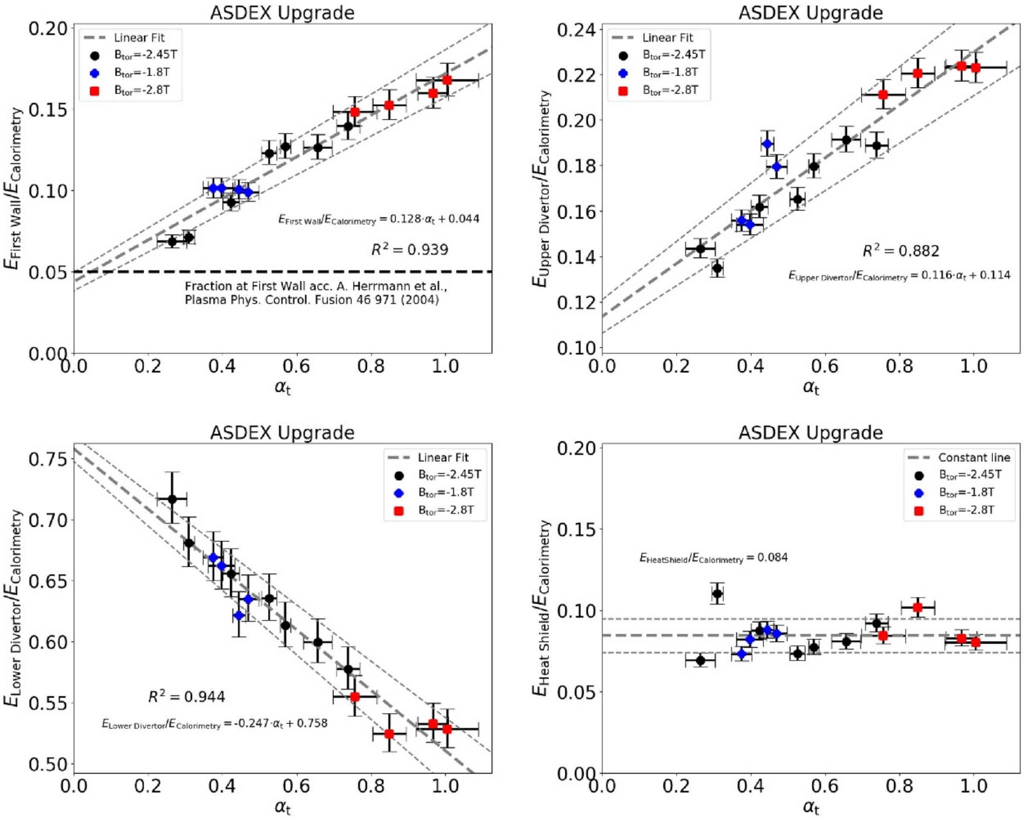

Figure 7. The evolution of the PFC heat loads at the first wall (left top), the upper divertor (right top), the lower divertor (left bottom) and the central heat shield (right bottom). Reprinted from [29], Copyright (2023), with permission from Elsevier.

This scaling is extended to all area connected to the cooling water calorimetry. Figure 7 illustrates the evolution of the energy loads at the upper divertor (right top), at the lower divertor (left bottom) and at the heat shield (right bottom). For both the upper and lower divertor, the correlation parameter R^2 and the regression formula with respect to α_t are added. The regression coefficient R^2 show for both the areas a reasonable correlation and supporting the observation with respect to the first wall scaling. Interestingly, the slopes of both regressions, the upper divertor and the first wall, point out that the energy loads are equally transferred to both areas. A reduction of the energy deposited at the main divertor target would support the speculations of a further energy loss channel carried by turbulent structures/ballooning modes at the separatrix. This has already been checked by means of thermocouple measurements at the divertor target in [29] supporting this picture.

As reported in [1] by using IR-thermography, the energy loads in the upper divertor increases whenever the QCE-regime is achieved. As the upper divertor is not connected with the main plasma, the increase of energy loads is associated with an increase of cross-field transport [1]. The tomographic reconstructions and poloidal radiative heat load distributions of discharge #39231 in [35] indicate a strong localised radiation pattern between the upper X-point and the upper divertor plates.

As the calorimetric observations suggest that the increase of energy loads at the upper divertor are connected with the increase of the separatrix turbulence described by α_t, the evolution of this additional, localised radiation pattern may follow this trend as well. Also the magnitude of the radiative energy loads reaching the upper divertor is of interest. The connection between filamentary transport and this localised radiation pattern at the upper divertor plates is yet not clear and requires further investigations.

To determine amount of radiative energy reaching the upper divertor, the framework based on CHERAB and a Gaussian-Processes-Tomograpic model has been exploited. This framework is introduced in [35].

In figure 8, the evolution of the radiative energy loads at the upper divertor normalised to the total energy load as inferred by the calorimetry $E_\mathrm{Calorimetry}$ is plotted against α_t. A reasonable trend between the normalised radiative energy loads and α_t can be observed. The regression formula and R^2 of this evolution is added. The slope of the radiative evolution matches well with the one from calorimetric measurements. Comparing figure 7 (top right) with figure 8, we recognise that the radiation contribution to upper divertor energy load is significant for the explored α_t-range, moving from about 56 % at lower α_t up to almost 80% at higher values.

Following [1], a certain contribution from parallel conductive transport is expected to be deposited at the upper divertor. The results from [29] suggest that the conductive contribution is significant at low α_t and decreases with increasing α_t. Figure 9 represents the evolution of the energy loads

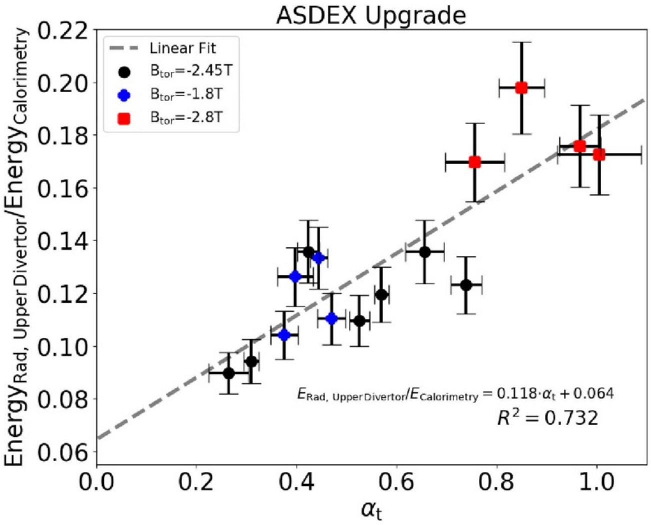

Figure 8. Evolution of the radiative heat loads reaching the upper divertor normalized by $E_{\mathrm{Calorimetry}}$ is plotted against α_t. A reasonable agreement between the radiation reaching the upper divertor and α_t is observed.

on *Tile 1*, *Tile 2* and *Tile 3* of the upper outer divertor following the labelling in figure 9(top). It is normalised by the total energy obtained from thermocouple measurements covering the entire upper divertor. The distributions of the inner divertor tiles reveal no substantial variations throughout the whole database and therefore they are not shown. *Tile 1* is the tile which is expected to be dominantly exposed to the parallel conductive transport. For lower α_t, a larger fraction of the total energy reaching the entire upper divertor is deposited at *Tile 1* than for higher α_t. Simultaneously, an increase of the fraction of deposited energy can be observed for *Tile 2* and *Tile 3* with increasing α_t. The slope of both tiles matches to the slope of *Tile 1*. Following the conclusions previously drawn in [29], the reduction at *Tile 1* may be accompanied by a reduction of the parallel transport causing a change in the energy distribution of the upper divertor. It cannot be excluded that due to the λ_q-broadening reported in [1], a fraction of the parallel conductive transport reaches a neighboring tile in the upper divertor and thus (additionally) influences the energy distribution.

It can only be speculated, how this localised radiation pattern is connected with α_t. Further investigations on that phenomena are needed, in particular for further devices, in order to understand the link between the CDN-magnetic field configuration, first wall geometry and PFC material.

3.2. Generalization of first wall energy load scaling

It is of great interest whether the observed trend at the first wall can be extended to further discharges. A selection of discharges with different plasma characteristics have been added to the database. Each discharge provides several separatrix data points. For each discharge, the mean value of the separatrix values from the flattop phase are used to determine α_t. The table 1 summarizes the characteristics of the database

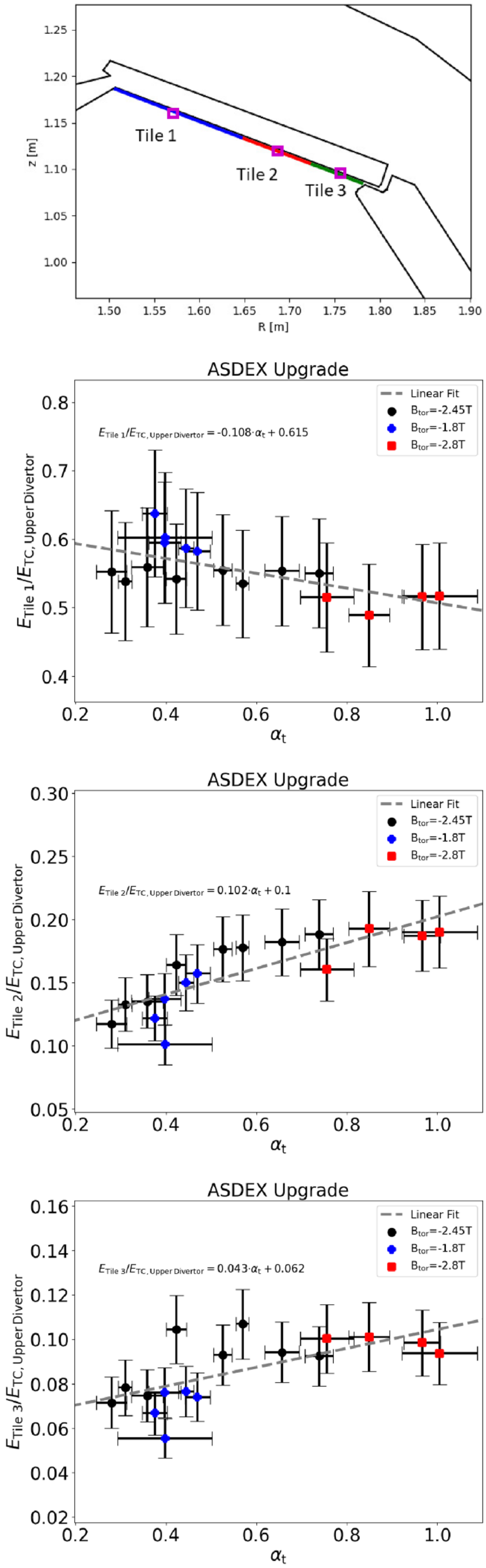

Figure 9. Top: distribution of the three relevant tiles in the upper outer divertor. Evolution of the energy load distribution for the three tiles of the upper outer divertor normalized by $E_{\mathrm{TC,Upper\,Divertor}}$ is plotted against α_t.

Table 1. Overview of the selected discharges with their properties to extend the first wall energy load scaling in figure 10.

Plot label	I_p (MA)	$\lvert B_{tor}\rvert$ (T)	P_{tot} (MW)	D_{tot} [10^{22} s^{-1}]	δ_u	κ
QCE with $\lvert B_{tor}\rvert \leqslant 1.9$ T	0.8–0.94	1.9–1.5	NBI: 7.5–5.0 ICRH: 4.0–0.0	1.0–4.0	0.31	1.65–1.81
QCE with max. $n_{e,sep}$	0.8	2.5	NBI: 12.5–7.5 ICRH: 4	5.0–5.5 (with additional pellet fuelling)	0.31	1.66
L-H-L high density discharge	0.8	2.5	NBI: 7.5–5 ECRH: 1.5	0.15–10.6	0.075	1.64
Low density H-mode + pellet	0.8	2.5	NBI: 4–10 ECRH: 3.6	1.0–0.5 (with additional pellet fuelling)	0.1–0.3	1.68–1.60
HDL discharge	0.8	2.5	NBI: 2.5–5 ECRH: 0–3.2	0.9–3.0	0.29 1.66	

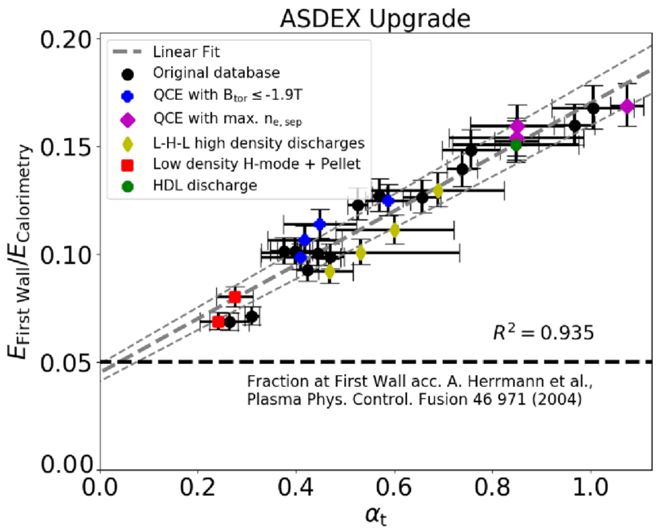

Figure 10. Evolution of the first wall energy loads considering further AUG discharges. The different color markers correspond to the entries in table 1. The linear trend by using α_t is preserved which is emphasized by the high value of R^2. The error-bars of the added discharges do not denote the uncertainty of the measurements, but the variation throughout the discharge.

extension and figure 10 visualizes the extension of the first wall energy load scaling. The scaling shows an almost ideal correlation with α_t indicated by a high R^2. It suggests that the different properties, at least for the first wall, do not have a large effect on the scaling.

The main challenge at AUG is the narrow spatial operational space of the edge TS in which shaping dependencies can be investigated. A scan of the position of the separatrix would be of great interest to confirm or refute the hypothesis of a filament decay length. To investigate these aspects, similar studies need to be performed on other machines with ITER-like-wall to identify further geometry/shaping dependencies. The extension to further machines would be also demanded to identify the actual upper limit for α_t. For low-δ plasma, the upper limit seems to be 1 [21], whereas for high-δ plasmas values larger than 1 can be achieved [3].

4. The evolution of upstream and downstream SOL profiles

The evolution of energy distribution at the PFCs in AUG shown and discussed in the previous section shows promising trends. A significant fraction of the energy can be deposited on non-divertor components, namely the first wall and the upper divertor. It is now of interest to investigate, how the SOL profiles change within the database.

Firstly, the evolution of the divertor heat flux profiles by means of IR-thermography is discussed. Figure 11 shows the divertor heat flux profiles for a set of AUG discharges conducted at $B_{tor} = -2.45$ T. In this analysis, f_x is set to 5.0. The legend denotes the different discharges with the respective quantities, the power fall-off length λ_q and the divertor broadening S, in descending ordering with respect to the normalised separatrix density in terms of n_{GW}. The two cases with lowest fuelling (#40 240 and #39 523) are ELM-filtered and illustrate only the Inter-ELM profiles. In subsequent plots, the same color code is used for the $B_{tor} = -2.45$ T subset.

The background obtained from the Eich-fit is removed for this study in order to avoid discrepancies due to negative background values after Type-I ELM crashes caused by the implied energy conservation in THEODOR [32]. The background heat flux is for most discharges in the order of 0.5 MW m^{-2}. As ELMs are not considered, only the profiles at higher fuelling represents the total power reaching the target. As reported in [1, 3, 16], with increasing fuelling a continuous increase of λ_q and S is witnessed. In case of #40 240 and #40 241, S does not perfectly match to this trend,

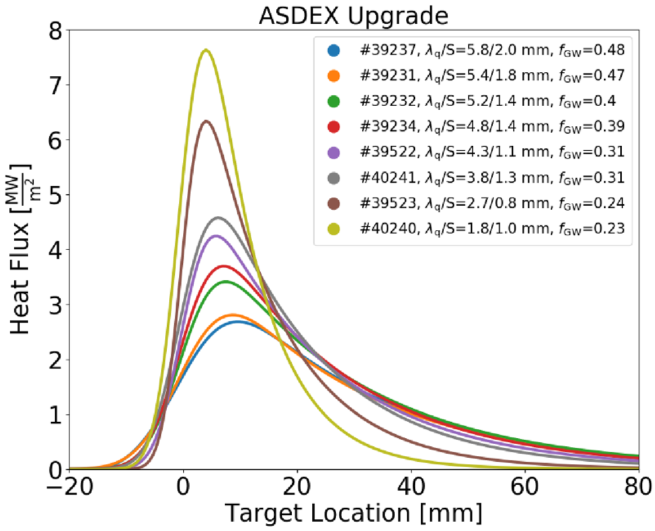

Figure 11. Heat flux profiles measured with the IR-thermography at the main target. λ_q and S are remapped to the OMP. The strikeline position and the background heat flux (taken from the Eich-fit) are subtracted from all profiles. The legend illustrates the order of discharges by exploiting the achieved separatrix density, which is normalised by the Greenwald density n_{GW} ($\approx 10^{20}$ m^{-3}). In case of the two lowest flattop fuelling cases being in dominating Type-I ELM H-mode, only the Inter-ELM profiles are shown.

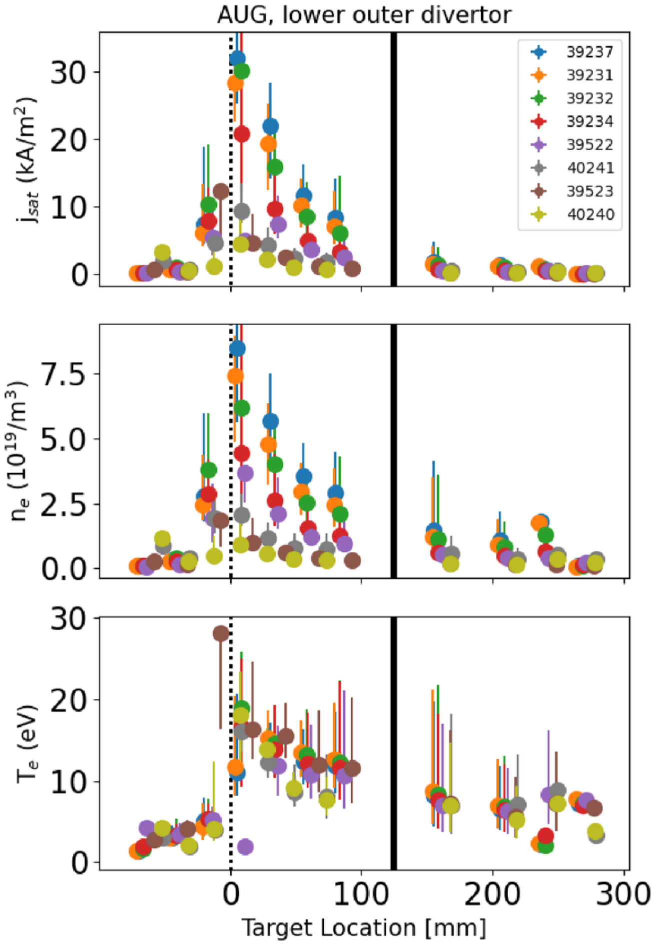

Figure 12. LP profiles for $B_{\mathrm{tor}} = -2.45$ T are ELM-filtered and each probe along the divertor coordinate is median-averaged over a time interval of ~ 1 s. The error-bars denote the standard deviation. The plots illustrate the ion saturation current density j_{sat} (top), the electron density n_e (middle) and the electron temperature T_e (bottom) at the main target (*Tile 1*, left side of black vertical line) and *Tile 2* (right side of black vertical line).

as the T_e on the divertor target tile is slightly different as proven by the LP measurements shown in figure 12 [69]. Even though the low density cases represent only parts of the total power reaching the target, still a reduction of the peak heat flux is observed with increasing fuelling which is beneficial for the ITER divertor peak heat flux limits. λ_q increases by a factor of 3, S by a factor of 2, whereas the peak heat flux is reduced from ~ 8 MW m^{-2} to below 3 MW m^{-2} at maximum fuelling. Combining this observation with the trend reported in [29], one can conclude that an increase of α_t seems to be associated with a reduction of the parallel conductive transport to the target and a simultaneous reduction of the peak heat flux.

The evolution of λ_q in QCE-phase follows the regression introduced in [3] which suggests a correlation with $n_{e,\mathrm{sep}}$ or the separatrix pressure $p_{e,\mathrm{sep}}$. Recent studies from TCV [16] suggest rather a reasonable trend of λ_q with α_t. These diverse observations require an extension of the QCE scenario to further devices, in order to provide further insights in the for ITER beneficial λ_q-broadening.

The corresponding LP-measurements are provided in figure 12. The LP profiles (j_{sat} (top), n_e (middle) and T_e (bottom)) illustrate the evolution for $B_{\mathrm{tor}} = -2.45$ T. The profiles are ELM-filtered and along the divertor coordinate each probe is median-averaged over a time interval of $\sim$1 s. The error-bars denote the standard deviation. The values from probes, which are close to the strikeline, might be negatively affected and have to be interpreted with care. The black vertical line denotes the separation between *Tile 1* (left side of the line) and *Tile 2* (right side of the line). For the first part of the discussion, the focus is on *Tile 1*. Starting with the bottom panel, it can be observed that throughout the entire fuelling scan the target T_e remains mostly constant for each discharge configuration. The top panel visualizing j_{sat} observe an increase of impinging particles, which is to be expected when a density shoulder formation is aimed for.

The observations concluded from calorimetric measurements are in contradiction to the heat flux derived from LP measurements. As illustrated in figure 13, a continuous increase of $q_\perp$ with increasing fuelling can be observed. The general form [70, 71] of the heat flux $q_\perp$ deduced from LP measurements can be written as:

$$q_\perp = q_{\mathrm{kin,i}} + q_{\mathrm{kin,e}} + q_{\mathrm{ref}} + q_{\mathrm{refl}}. \tag{14}$$

$q_\perp$ can be decomposed into four contributions: the ion/electron heat flux $q_{\mathrm{kin,j}}$, the recombination heat flux q_{ref} and the reflected heat flux q_{refl}. The kinetic electron contribution $q_{\mathrm{kin,e}}$ takes into account the impact of j_{net}, the electric current density

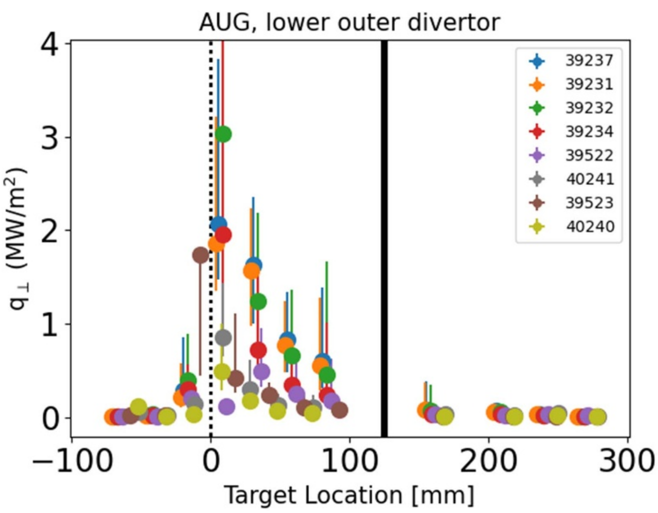

Figure 13. Evolution of $q_\perp$ from LP-measurements conducted at $B_{tor} = -2.45$ T.

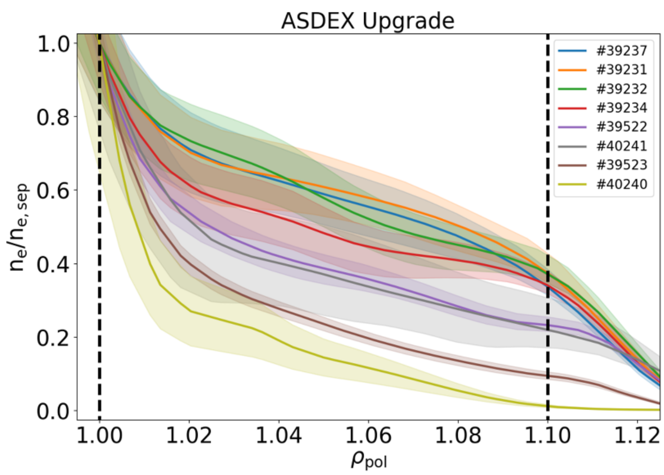

Figure 14. Evolution of the density shoulder measured by the LIB diagnostic for discharges conducted at $B_{tor} = -2.45$ T. The change of density in near- and far-SOL is solely caused by changing the flattop fuelling level.

to the target, following [71]. For most applications assuming $T_e = T_i = T$ and $j_{net} = 0$, equation (14) can be simplified to:

$$q_\perp = (\gamma T + E_{rec})\,\Gamma, \tag{15}$$

where γ denotes the sheath heat transmission coefficient, E_{rec} the sum of the ionization energy and the Franck–Condon dissociation energy per recycled ion and Γ the ambipolar ion particle flux to the wall. γ can be expressed as:

$$\gamma = [4.85\,(1 - R_E) + 2.15]\,, \tag{16}$$

using the numerical values reported in [70] and R_E being the ion reflection coefficient. For most electron temperatures, R_E can be set to 0.5 leading to a $\gamma \approx 4.5$. The prefactor R_N, describing the fraction of ions reflected from the target as neutrals, which may have a considerable impact on $q_\perp$ for high-recycling divertor conditions, which depends like R_E strongly on T_e presuming $T_e = T_i$. This observation requires further dedicated investigations which takes into account the proper values of T_e and T_i separately.

The thermocouple measurements at the outer divertor report on a reduction of the power reaching the divertor main target (*Tile 1*) presuming the energy loads on the baffle tile (*Tile 2*, right side of the black line figures 12 and 13) do not dramatically change. The proof of this presumption can barely be obtained, but checks with divertor LPs, IR and bolometry supporting the presumptions can be done.

The top panel of figure 12 illustrates j_{sat} which acts as a simple proxy for impinging charged particles. For Tile 2 (right side of the black vertical line) j_{sat} remains on a low level throughout the entire fuelling scan at $B_{tor} = -2.45$ T. The extrapolation of the IR-fit profiles to cover *Tile 2* in order to assess the impact of the λ_q-broadening leads to a similar conclusion. Parallel conductive heat flux is not transferred by λ_q-broadening to *Tile 2*. Also checks with bolometric measurements using the framework based on CHERAB and the GPT model provide provide no clear trend of radiative energy loads on *Tile 2*.

4.1. Quantification of the density shoulder amplitude in QCE H-modes

As reported in [15], achieving high $n_{e,sep}$ leads to a broadening of the *e*-folding temperature and density decay lengths λ_t and λ_n together with the formation of a density shoulder. The formation of a density shoulder is generally associated with an enhancement of filamentary activities in the far-SOL [1, 14, 16, 19, 20] and a common characteristic of the QCE-regime [1]. Figure 14 illustrates the evolution of the density in the near- and far-SOL exploiting LIB-measurements for database discharges conducted at $B_{tor} = -2.45$ T for which most LIB-measurements are available. The change of density in near- and far-SOL is solely caused by changing the flattop fuelling level. The density in the SOL is normalized by $n_{e,sep}$. The two vertical dashed lines denote the position of the separatrix ($\rho_{pol} = 1.0$) and the limiter tile surface ($\rho_{pol} = 1.1$) at the midplane. Throughout the database subset, a substantial variation of the SOL density can be observed. At the highest normalized SOL density, a saturation of the density amplitude appears.

To qualify the evolution of the density amplitude in the far-SOL, a qualifier is exploited which has been introduced in [18]. This procedure characterize the shoulder across the near- and far-SOL range by the subsequent definition:

$$\tilde{n}_e = \frac{\int_{1.0}^{1.1} n_e \mathrm{d}\rho_{pol}}{n_{e,sep}\Delta\rho_{pol}} = \frac{\langle n_e\rangle_{SOL}}{n_{e,sep}}, \tag{17}$$

where n_e denotes the electron density in the SOL, ρ_{pol} denotes the normalized poloidal flux coordinate and $\Delta\rho_{pol}$ the integration range with the magnetic coordinate. LIB-measurements which cover n_e in the near- and far-SOL, are available for most of the database discharges. The integration covers the range from 1.0 to 1.1 of ρ_{pol}.

The values obtained with the qualifier defined in equation (17) are visualized in figure 15 as solid markers. It can be seen that with varying the flattop fuelling level,

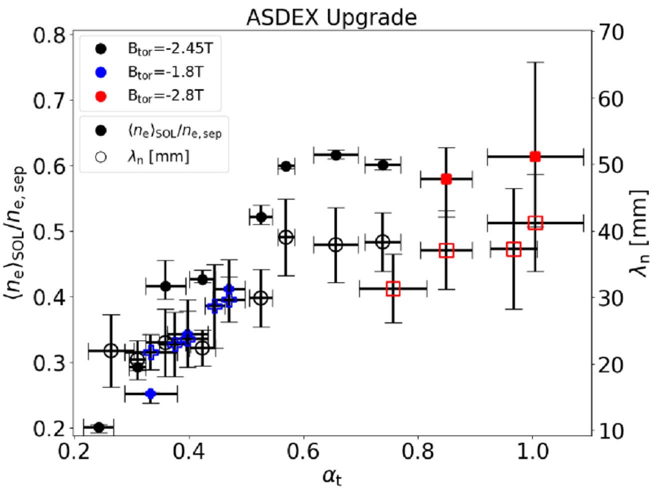

Figure 15. The density shoulder amplitude qualifier (solid markers) is plotted against α_t. Exceeding $\alpha_t \approx 0.55$, a saturation in the qualifier can be observed. The markers with no face-color visualize the evolution of *e*-folding density decay length λ_n obtained with the edge TS with respect to α_t.

the density shoulder qualifier increases continuously until α_t exceeds ≈ 0.55. Exceeding $\alpha_t \approx 0.55$ leads to a saturation of the density shoulder amplitude. The saturation threshold in α_t is similar to the limit introduced in [3] classifying an H-mode plasma into a Type-I ELMy H-mode and into a QCE H-mode. This observation suggests that a fully formed density shoulder might be connected with achieving a QCE H-mode and is in agreement with the observations from TCV for QCE H-modes observing also a saturation in the density shoulder amplitude above a critical value in α_t [16].

Additionally, the *e*-folding decay length λ_n obtained with the edge TS is plotted (markers with no face color) illustrating the behaviour of the near-SOL while forming the density shoulder. A similar trend as for the density shoulder qualifier is observed suggesting that the formation of the density shoulder is not only correlated with the properties in the far-SOL, but also still connected with the properties of the near-SOL suspecting a dependence on separatrix quantities. It is also important to note from figure 15 that despite the increase of far SOL density, the general shape of the density SOL profile is not substantially changed with a break between near and far SOL approximately around $\rho_p \approx 1.015$. This is not actually an universal features since different profile evolution is observed as density is increasing on TCV [16] or JET [19] and clearly further multi-machine investigation is needed to address this question but this topic is clearly beyond the present manuscript.

Of interest might be the position of the breakpoint classifying the SOL into near-a far-SOL. To determine the range of the near-SOL, we cannot apply the power balance approach as used for the edge TS. As reported in [72], the range between the extreme values of $\nabla^2 n_e$-profile determine the near-SOL range and is exploited for this analysis. The outer boundary of the near-SOL range is also denoted as breakpoint R_{break}. The far-SOL range is therefore defined between the outer boundary of the near-SOL range and the first wall PFC. The latter position is fixed at $R_{\mathrm{lim}} = 2.177$ m. To fit both ranges, near- and far-SOL, an exponential fit function of the following form is used:

$$f(x) = a \cdot e^{-b\cdot(x-c)} + d. \tag{18}$$

For this database, the near- and far-SOL profile can be fitted by the equation (18), respectively. Of rather importance might be the position of the breakpoint. The breakpoint, which is defined as the maximum-peak in the $\nabla^2 n_e$-profile is located between 1.25 and 1.7 cm in front of the separatrix. The secondary separatrix is for this magnetic equilibrium between 2.15 and 2.6 cm in front of the primary separatrix.

The formation of a density shoulder is generally associated with an increase of the neutral pressure in the SOL. Previous studies at TCV [16, 18], at AUG [73] and at JET [19, 20] have suspected the requirement of increased neutral pressure in the divertor to achieve the formation of a density shoulder in the far-SOL. On the other side, investigations in L-modes at TCV [74] have suggested a major role played by midplane neutral pressure.

Figure 16 illustrate the evolution of neutral pressure close to the upper divertor (top) and in the lower divertor (bottom) being measured below the roof baffle. Both measurements are plotted against α_t. The top plot indicate a clear correlation between α_t and the upper divertor neutral pressure, whereas the divertor neutral pressure increases with α_t, but demands a different dependence on $q_{\mathrm{cyl}}/B_{\mathrm{tor}}$ indicating a missing connection between separatrix and divertor conditions. The upper divertor baratron provides high neutral pressure values which might be affected by its close position to the upper divertor and the localised radiation pattern in the upper divertor as discussed before.

The trends of both baratrons are in agreement with the trends observed by the manometers measuring the neutral flux density of the upper divertor and main chamber and the manometer acqwuiring the neutral flux density in the roof baffle.

5. The radial filamentary heat transport in high-δ discharges

5.1. Determination of the filamentary heat flux using probe measurements

Dedicated probe measurements were executed in most discharges to derive the quantities describing the filament characteristics. The derived quantities from both probe-heads can also be used to determine the radial filamentary heat flux associated to filaments. The expression describing this radial convective transport, has been introduced in [53] and applied on AUG high-density L-mode discharges:

$$q_{\mathrm{r,fil}}^{\mathrm{total}} = q_{\mathrm{r,fil}}^{\mathrm{electron}} + q_{\mathrm{r,fil}}^{\mathrm{ion}} = \frac{5}{2}\Gamma_{\mathrm{r,fil}} T_{\mathrm{e,fil}} + \frac{1}{2}\Gamma_{\mathrm{r,fil}}\left[5T_{\mathrm{i,fil}} + m_{\mathrm{i}}\left(c_{\mathrm{s}} M_{\parallel}\right)^2\right]. \tag{19}$$

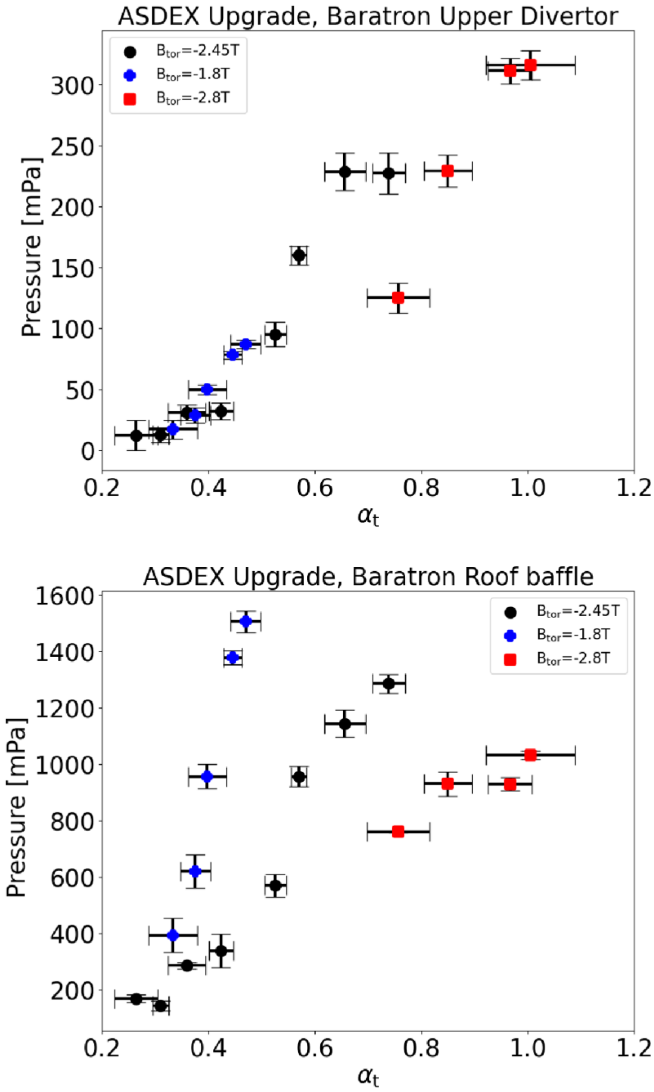

Figure 16. Top: the neutral pressure measured close to the upper divertor is plotted against α_t. A reasonable agreement is observable indicating a connection between the turbulence activity at separatrix and the neutral pressure in the SOL. Bottom: the neutral pressure measured at the roof baffle is plotted against α_t. A correlation with a different dependence on q_{cyl}/B_{tor} is observed indicating a missing connection between separatrix and divertor conditions.

The radial filamentary heat transport consists of an electron $q^{\text{electron}}_{\text{r,fil}}$ and an ion contribution $q^{\text{ion}}_{\text{r,fil}}$. Contributions parallel and perpendicular to the magnetic fields contribute to the radial heat transport. The perpendicular contribution is given by $\frac{5}{2}\Gamma_{\text{r,fil}}T_{\text{j,fil}}$. The parallel contribution is deduced from the inertia term in the energy conservation and only its ion contribution is considered due to $m_e << m_i$. It is approximated by $\frac{1}{2}\Gamma_{\text{r,fil}}m_i(c_s M_{||})^2$. As discussed in section 2.1, the RFA2 sweeping frequency at 5 kHz was not sufficient to estimate $T_{\text{i,fil}}$. The obtained values are averaged over filaments and represent the background ion temperature $T_{\text{i,RFA2}} = T_{\text{i,BG}}$. In [53], it has been reported that in high-density L-mode discharges

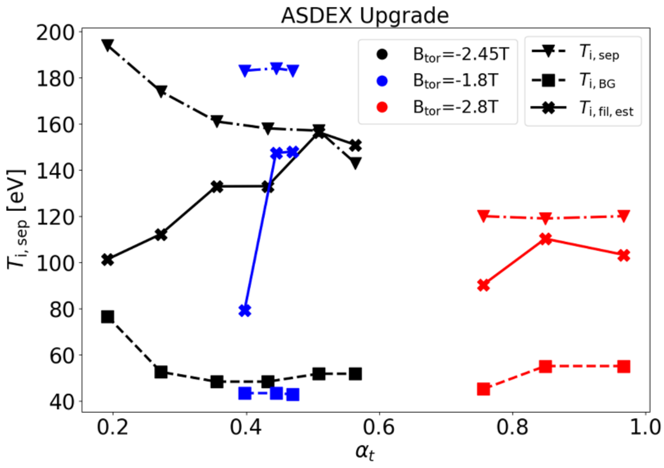

Figure 17. Illustration of the range of $T_{\text{i,fil,est}}$ within its lower and upper boundary given by $T_{\text{i,sep}}$ from IDI and $T_{\text{i,BG}}$ from the RFA2.

$T_{\text{i,fil}}$ is in the range of $T_{\text{i,BG}}$. Given the lack of similar information concerning H-mode, we are assuming that the ion temperature relative fluctuation scales similarly to the electron one, thus assuming:

$$\frac{T_{\text{i,fil}}}{T_{\text{i,BG}}} = \frac{T_{\text{e,fil}}}{T_{\text{e,BG}}}, \tag{20}$$

The values of the estimated filament ion temperature $T_{\text{i,fil,est}}$ are illustrated in figure 17. The estimated values are within the boundaries given by IDI-profiles based on CXRS-measurements at the separatrix and given by the RFA2. The magnitude at lowest α_t representing Inter-ELM $T_{\text{i,fil}}$ is in agreement with previous studies conducted at AUG exploiting the RFA2 [48, 75, 76]. For higher α_t, $T_{\text{i,fil,est}}$ tends to $T_{\text{i,sep}}$. However, no references for QCE-$T_{\text{i,fil}}$ are known to compare them with $T_{\text{i,fil,est}}$.

Figure 18 provides an overview of the quantities derived from the BPP measurements. This analysis excludes the evaluation of ELMs, as the acquired profiles were not sufficient to deduce robust quantities from ELM-averaged I-V curves. All quantities are plotted against α_t. Furthermore, to estimate $n_{\text{e,BG}}$ and $n_{\text{e,fil}}$ following equation (8), the T_i-values of filaments and background plasma introduced before are utilized.

The filament packing fraction $f_{\text{PF,fil}}$ which has been introduced in equation (11) is illustrated in panel (*c*) and depends on the quantities shown in panel (*a*) and (*b*). The continuous increase of $f_{\text{PF,fil}}$ is triggered only by the growth of ν_{detect}, which represents the number of detected filaments within a certain time interval, whereas at the same time the correlation time τ reveals no substantial variations when QCE-filaments start to dominate the SOL transport. As τ is a proxy for the filament size (at least for the radial dimension assuming "frozen turbulence hypothesis"), it additionally suggests that Inter-ELM filaments are larger than QCE-filaments. Due to the lack of poloidal velocity measurements, further conclusions cannot be drawn.

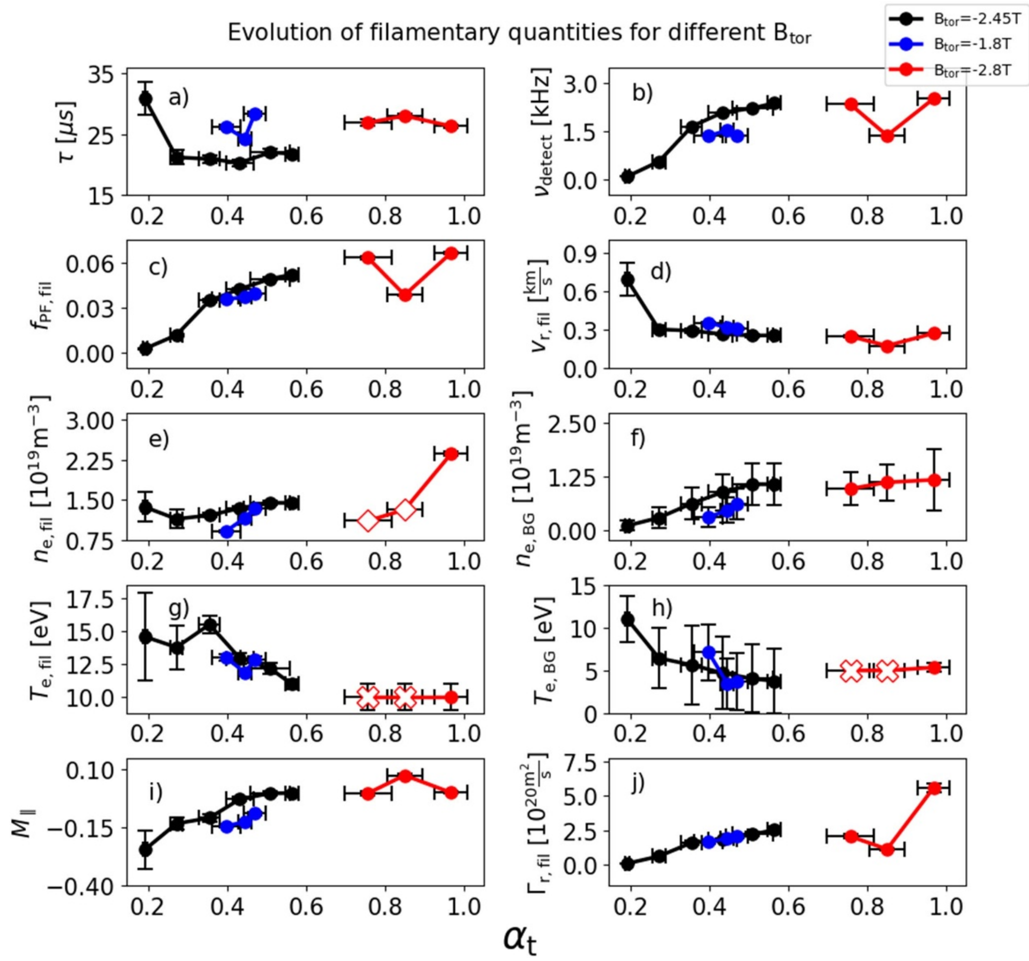

Figure 18. Overview of the filamentary quantities obtained with the BPP plotted against α_t: (*a*) the filament correlation time, (*b*) the filament detection frequency, (*c*) filamentary packing fraction, (*d*) the filamentary radial velocity, (*e*) the filamentary electron density, (*f*) the background electron density, (*g*) the filamentary electron temperature, (*h*) the background electron temperature, (*i*) the filamentary parallel Mach number, (*j*) the filamentary particle flux.

Interestingly, the radial filament velocity $v_{\mathrm{r,fil}}$ at the first wall shown in panel (*d*) is lower for QCE filaments than for Inter-ELM filaments and also reveals only slight variations when the QCE-phase has been achieved. This seems to be in contradiction to previous studies conducted in AUG using the thermal Helium Beam diagnostic [13] and at TCV using a reciprocating probe [16]. With respect to the density shoulder observations discussed in section 4.1, it can also be concluded that the mechanism behind the density shoulder formation seems not to be linked to the far-SOL filament radial velocity $v_{\mathrm{r,fil}}$, which is in contrast to previous assumptions [77].

Together with the observations in panels (*e*) and (*g*) and in figure 17 visualizing the filamentary electron density, electron temperature and ion temperature, one can conclude that the enhancement of convective transport is carried by more frequently generated and denser filaments and not by an increase of the ion or electron temperature. The two diamond red markers for $n_{\mathrm{e,fil}}$ denote results where the I_{sat} fluctuation went above the analog-to-digital converter resolution. As a consequence, $n_{\mathrm{e,fil}}$ are for those two cases likely underestimated. The two red crosses for $T_{\mathrm{e,fil}}$ and T_{BG} denotes cases, where ϕ_{f} was somehow corrupted and the corresponding temperature values are taken from the remaining discharge conducted at $B_{\mathrm{tor}} = -2.8$ T.

The evolution of $M_{\parallel}$ is shown in panel (*i*). Its behaviour converging to 0 with increasing α_t seems to be in agreement with recent numerical GBS simulations at TCV [78] realised for high-density L-mode discharges. The sign of $M_{\parallel}$ is negative meaning the parallel contribution reaches the outer divertor. Following the definition of $\Gamma_{\mathrm{r,fil}}$ from equation (11) and illustrated in panel (*j*), it can be concluded that the particle flux carries mostly the enhancement of filamentary transport in high-δ discharges.

Figure 19 illustrate the evolution of the perpendicular, parallel and total heat flux associated with filaments. The trend of the perpendicular filamentary heat flux $q_{\mathrm{r,fil}}^{\mathrm{perp}}$ shown in top plot is dominated by $\Gamma_{\mathrm{r,fil}}$. The middle plot visualizes the parallel contribution. Over the entire range, this contribution is negligible. The bottom plot illustrates $q_{\mathrm{r,fil}}^{\mathrm{total}}$ as defined in equation (19).

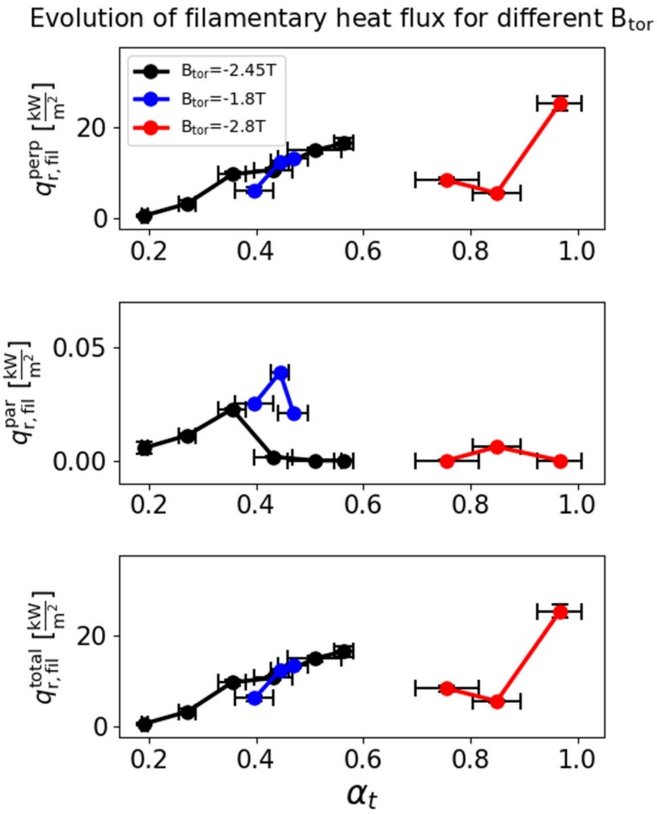

Figure 19. Contributions to radial filamentary heat flux: Top: the filamentary perpendicular heat flux, middle: the filamentary parallel heat flux, bottom: the filamentary total heat flux.

5.2. Comparison of $q^{\text{total}}_{\text{r,fil}}$ with $q_{\text{Calorimetry}}$

In the previous section, the convective heat flux associated with filaments has been determined using probe measurements which were performed close to the first wall. These results can now be compared with the calorimetric results to estimate the magnitude of the filamentary contribution to the total heat flux reaching the first wall caused by particle transport. The averaged heat flux reaching the first wall, $q_{\text{Calorimetry, First Wall}}$, can be estimated by:

$$q_{\text{Calorimetry, First Wall}} = \frac{E_{\text{Calorimetry, First Wall}} - E_{\text{Rad, First Wall}}}{t_{\text{Plasma}} \cdot A_{\text{First Wall}}}. \quad (21)$$

$E_{\text{Calorimetry, First Wall}}$ denotes the calorimetrically acquired energy of the 8 cooling units defining the first wall, $E_{\text{Rad, First Wall}}$ the radiative energy reaching the first wall, t_{Plasma} the duration of the flattop phase of the respective discharge, which is about $\approx$ 6 s, and $A_{\text{First Wall}}$ the surface area of the AUG first wall, which consists of the 4 ICRH antennas and the 4 auxiliary limiters, is $\approx$4.6 m^2. The calorimetry cannot differentiate the sources of energy loads on the PFCs. Therefore, the workflow based on CHERAB and the GPT model introduced in [35] is exploited in order to determine the incident radiation energy on the first wall. The term $(E_{\text{Calorimetry, First Wall}} - E_{\text{Rad, First Wall}})$ summarizes the energy loads on the first wall, which are caused by all particle transport present in the SOL. The evolution of this quantity is shown in figure 20. Even after the subtraction of $E_{\text{Rad, First Wall}}$, a reasonable trend is preserved covering the conclusion drawn in figure 7 (top left). Remarkably, the regression matches almost perfectly with the origin supporting the picture that α_t may properly describe the turbulent activities close to the separatrix.

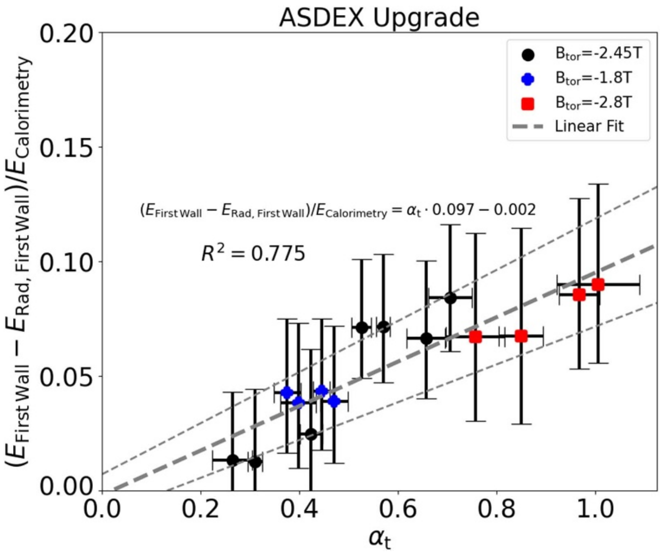

Figure 20. The energy loads from the first wall without the radiative energy loads are plotted against α_t.

Additionally, an averaged $q^{\text{total,av}}_{\text{r,fil}}$ has to be determined. As filaments are of ballooning origin, they occur only around LFS midplane, where the curvature of the plasma is unfavourable. As the filamentary activity correspond to the position, it can be assumed that the activities increase closer to the OMP at $z = 0.0$ m reaching its maximum. $q^{\text{total}}_{\text{r,fil}}$ obtained at the MEM position is at the OMP increased by the factor $\cos(\pi/6)$ following the argumentation in [53]. As $q_{\text{Calorimetry, First Wall}}$ corresponds to a poloidally averaged heat flux, $q^{\text{total,mid}}_{\text{r,fil}}$ must also be poloidally averaged. The maximum poloidal angle $\theta_{\max}$ is assumed to be $\pi/3$ following [53] with respect to the poloidal angle at the OMP as $\theta_0 = 0°$. $q^{\text{total,av}}_{\text{r,fil}}$ is obtained by the expression:

$$q^{\text{total,av}}_{\text{r,fil}} = \frac{\int_{-\pi/3}^{\pi/3} q^{\text{total,mid}}_{\text{r,fil}} \cos(\theta) \, d\theta}{\int_{-\pi/3}^{\pi/3} d\theta}. \quad (22)$$

The comparison between both heat fluxes are illustrated in figure 21. The results suggest that filaments contribute up to 25 % to the total particle-related heat flux reaching the first wall presuming $T_{\text{i,fil,est}}$ is in a realistic magnitude. Even at lowest α_t corresponding to the filamentary activities of low density H-modes, the filamentary contribution is non-negligible. Furthermore, the case, where $T_e = T_i$ has been assumed for equation 8, is added as grey shaded markers, For this case, the filaments would contribute up to 50% to the total heatflux reaching the first wall emphasizing the need of reliable T_i-values for studies at the first wall.

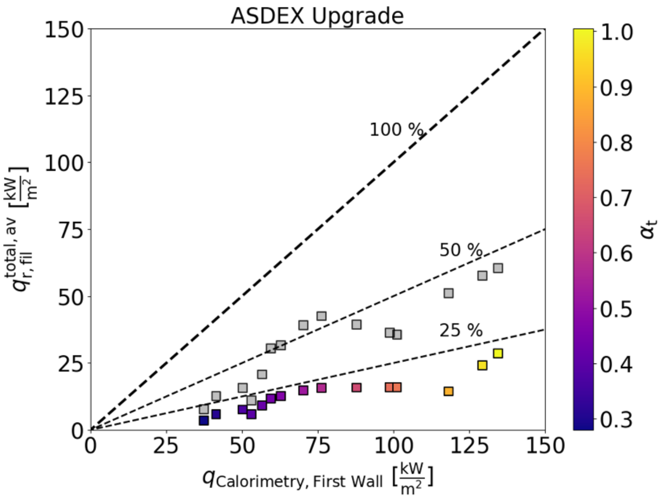

Figure 21. Comparison between the averaged heat flux reaching the first wall estimated by means of the AUG cooling water calorimetry and the filamentary heat flux based on probe measurements. The three dashed lines represent he case of 25 %–, 50 %–, 100%–contribution of $q_{\rm r,conv}$ with respect to $q_{\rm Calorimetry,\,First\,Wall}$. The colored markers indicate the filament heatflux, for which $T_{\rm i,BG}$ and $T_{\rm i,fil}$ from the RFA2 has been utilized in equation (8), whereas the grey shaded markers illustrate the case, where $T_{\rm e}=T_{\rm i}$ has been assumed for equation 8.

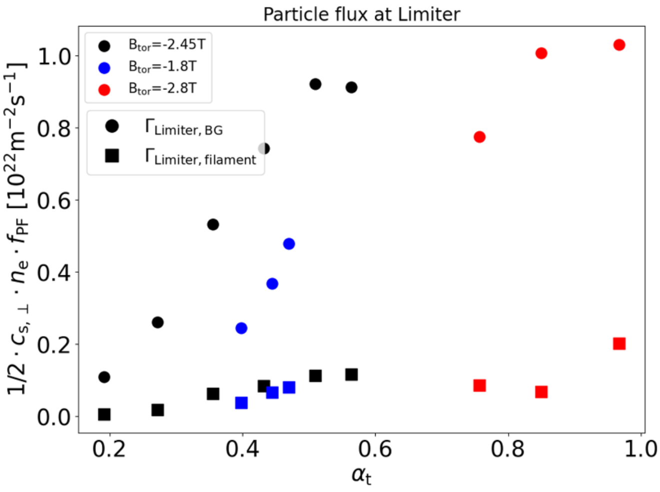

Figure 22. Illustration of the particle flux $\Gamma_{\rm Limiter}$ reaching the limiter.

5.3. Estimation of the gross erosion at the AUG first wall

The availability of limiter probe measurements allows to estimate the filament and background induced gross erosion at the AUG first wall. The estimation of the gross erosion presented here is based on a simplified model introduced in [27, 42] and does not cover all erosion processes (e.g. prompt redeposition is not considered). The deduced values for the first wall tile gross erosion represent the estimated gross erosion at the position, where they have been acquired. They do not represent the gross erosion for the entire first wall. Following [27, 42, 52], the gross erosion can be expressed by:

$$E_{\rm gross}=\frac{1}{2}\cdot c_{\rm s,\perp}\cdot n_{\rm e}\cdot Y_{\rm Yamamura}\cdot f_{\rm PF}\cdot \Delta t/n_{\rm PFC}. \tag{23}$$

$Y_{\rm Yamamura}$ denotes the Yamamura sputtering yield [79], $n_{\rm PFC}$ the PFC material density, Δt the exposure time and $f_{\rm PF}$ the packing fraction. In contrast to the study in [27], $f_{\rm PF}$ is considered for both contributions, background plasma and filaments. The time period, which is not occupied by filaments, is associated to the background contribution and is simply obtained by subtracting $f_{\rm PF}$ from 1. The exposure time Δt is set to $31.5\cdot 10^6$ s corresponding to a full year of plasma operation. For tungsten, $n_{\rm PFC}$ is set to $6.3\cdot 10^{28}$ m^{-3}.

The term $\frac{1}{2}\cdot c_{\rm s,\perp}\cdot n_{\rm e}\cdot f_{\rm PF}$ (dubbed $\Gamma_{\rm Limiter}$) denotes the perpendicular particle flux. The erosion on main chamber tiles is carried by the perpendicular projection $c_{\rm s,\perp}$ of the ion speed sound $c_{\rm s}$, which can be approximated by:

$$c_{\rm s,\perp}\approx c_{\rm s}\cdot \sin(\beta), \tag{24}$$

where β denotes the angle of the perpendicular velocity contribution with respect to the total velocity contribution. [80, 81] suggest that such cross-field transport arises at shallow field line inclinations. However, the inclination of the magnetic field lines along limiter tiles varies with its position and is therefore a non-constant parameter. For this simplified estimate, the corresponding angle β describing the perpendicular contributions is supposed to be 2°. Cross-field transport seems to occur at low field angle inclinations [80, 81]. Figure 22 illustrates the evolution of $\Gamma_{\rm Limiter}$ for the available probe measurements. The background particle flux $\Gamma_{\rm Limiter,BG}$ increases stronger than the filament particle flux $\Gamma_{\rm Limiter,filament}$. A saturation of $\Gamma_{\rm Limiter,BG}$ is observed, when $\alpha_{\rm t}$ exceeds 0.55.

$Y_{\rm Yamamura}$ describes the sputtering yield ('number of PFC atoms expelled per incident ion from the plasma') following the definition in [79] and is a non-linear function of the electron and ion temperature. $Y_{\rm Yamamura}$ is based on the the revised Bohdansky formula [82], which also takes into account the angle α between the trajectory vector of the incident ion and the PFC surface normal vector at the impact position. At AUG, α is typically $\approx 60°$ for D^+ [83]. $Y_{\rm Yamamura}$ can be expressed as:

$$Y_{\rm Yamamura}(E_0,\alpha)=Y_{\rm Bohdansky}(E_0,\alpha=0°)(\cos\alpha)^{-f} \times\exp\left(f[1-(\cos\alpha)^{-1}\cos\alpha_{\rm opt}\right), \tag{25}$$

where E_0 is the projectile energy and f and $\alpha_{\rm opt}$ are used as fitting parameters. For f and $\alpha_{\rm opt}$, the same values are used, 1.46 and 82.3°, respectively. The values correspond to the sputtering of H on W. The determination of Y is based on results summarized in [84]. To determine $Y_{\rm Yamamura}$, it is assumed that the ions are Maxwellian distributed which leads to the following expression for E_0:

$$E_0=2k_{\rm B}T_{\rm i}-ZeV_{\rm S}, \tag{26}$$

where the first term denotes the approximated thermal energy of ions and the second one the energy of a single ion with

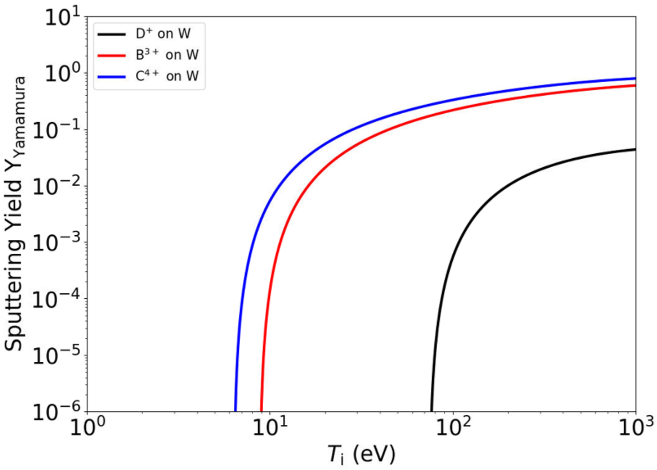

Figure 23. The sputtering yield Y on a tungsten surface for different incident ion species (D^+, B^{3+} and C^{4+}) is plotted against the ion temperatures assuming $T_i = 3 \cdot T_e$. X- and y-axis use logarithmic scale.

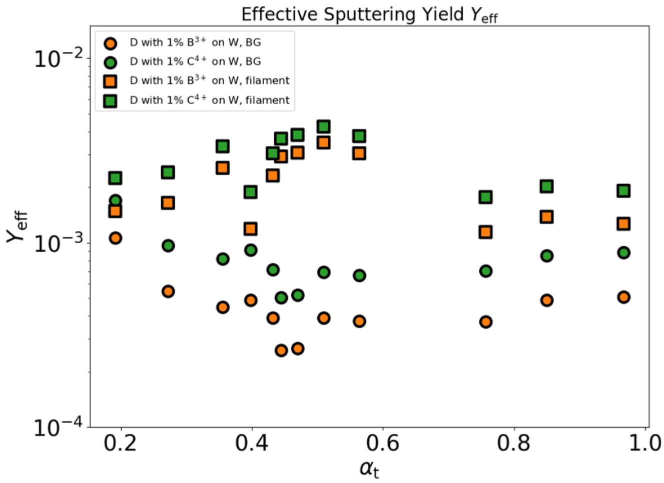

Figure 24. The effective sputtering yield Y_{eff} according to the definition in equation (28). Y_{eff} of background and of filaments are shown for two impurity species: B^{3+} and C^{4+}.

charge Z gained at the sheath potential drop V_S. V_S is negative for floating conditions and can be written in terms of $k_B T_e$ as:

$$\frac{eV_S}{k_B T_e} = 0.5 \cdot \ln\left[\left(2\pi\frac{m_e}{m_i}\right)\left(1+\frac{T_i}{T_e}\right)(1-\delta_{SEE})^{-2}\right], \quad (27)$$

where δ_{SEE} denotes the secondary electron emission coefficient. At $\delta_{SEE} = 0$, the ideal sheath potential is foreseen with $V_S \approx 2.5 k_B T_e / e$, whereas at e.g $\delta_{SEE} = 0.775$ V_s can drop to $k_B T_e / e$ reducing the acceleration of the ions in the sheath and consequently reducing the induced gross erosion. Following [85], the range of T_i suggests to set δ_{SEE} to 0.

In figure 23, the sputtering yields Y on tungsten for 3 species assuming $T_i = 3 \cdot T_e$ are visualized: D^+, B^{3+} and C^{4+}. The latter impurity was used in [27]. Focusing on the case with deuterium only (black line), one can see that Y becomes only important for T_i above a threshold of 100 eV. This threshold can only be exceeded by very hot filaments, which is given only for a small subset of the available measurements presupposing that $T_{i,fil,est}$ is in a realistic magnitude. Sputtering yields of possible impurities, here B^{3+} and C^{4+}, become already important at lower T_i. For the cases presented here, the thresholds are around 10 eV. Just from the sputtering yields, one can conclude that neither a pure deuterium background plasma nor filaments (excluding extremely hot filaments) would cause any gross erosion on tungsten. Gross erosion would only become important by the presence of impurities in the far-SOL.

To fill up equation (23) with both contributions, the values presented in figures 17, 18 and 23 are considered. To consider impurities, Y must be weighted accordingly to their assumed fractions in the plasma. The sputtering yield is weighted as followed:

$$Y_{eff} = \frac{\sum_j Y_j \cdot n_j}{n_e}, \quad (28)$$

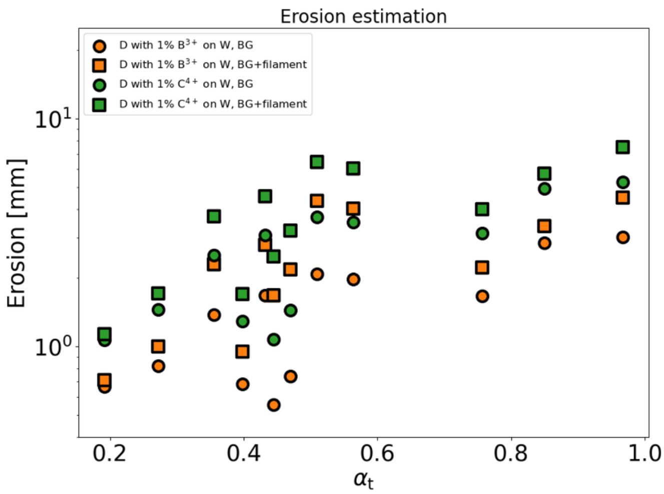

Figure 25. Estimated gross erosion for an exposure time Δt of one burn year (24 h/7d operation) for AUG H-modes. Above $\alpha_t \approx 0.55$ achieving the QCE scenario, the gross erosion saturates. The gross erosion is dominated by the background plasma associated to the density shoulder. The contribution from filaments can be significant, but they never dominate the total gross erosion. The y-axis uses a logarithmic scale.

where Y_j denotes the sputtering yield and n_j the density of the jth-species. n_e represents the electron density of filaments or background. Figure 24 illustrates Y_{eff} for all available probe measurements. The different Y_{eff} illustrate the contribution of filaments and background for two impurity species suggested before. Figure 25 illustrates the results for the gross erosion induced solely by the background (circle markers) and by both (square markers) for AUG operation conditions. At lowest α_t, representing the inter-ELM phase of a Type-I ELMy H-mode, the estimated erosion yields a magnitude of between 0.7 and 1.2 mm depending on the impurity species. The gross erosion at lowest α_t is dominated by the background plasma. Filaments would only cause a gross erosion below 0.1 mm.

With increasing α_t the estimated erosion increases continuously until α_t exceeds 0.55, which is similar to the condition to distinguish Type-I ELMy H-modes from QCE H-modes as introduced in [3]. Exceeding this value, the gross erosion saturates. The estimated erosion varies between 3.0 mm and 7.5 mm depending on the impurity species. Even in this range of α_t, the erosion is still dominated by the background plasma which is consistent with previous observations summarized in [27] for high-density L-modes AUG discharges. Replacing $T_{i,fil,est}$ by $T_{i,sep}$ or $T_{i,BG}$, the contribution of filaments varies only slightly. The wetted area exposed to the gross erosion can be approximated by:

$$A_{wetted} = \lambda_\Gamma^2 \cdot N / (\sin(\beta)\cos(\gamma)), \tag{29}$$

where λ_Γ denotes the particle flux decay length, N the number of ICRH limiter edges, which is 8, and γ the inclination between the parallel particle flux and the surface normal of the ICRH edge tile, which is about 15°. β has already been introduced describing the inclination of the particle flux along the tile surface and is about 2°. λ_Γ can be obtained from the MEM measurements, which suggests a decay length between 0.5 and 1.0 cm. Here, a value of 0.75 cm is considered. Inserting these values into the expression for A_{wetted} suggests a wetted area of about 0.13 m^2.

6. Summary

An extensive analysis of the SOL-profiles and of the heat flux evolution in high-δ discharges in AUG have been presented. The focus is on correlating SOL-profiles with the energy load distribution. The database covers a large range of AUG density operational space including as well variation of q_{cyl} obtained by changing B_{tor}. With increasing fuelling a gradual transition from Type-I ELMy H-mode to QCE H-mode has been observed achieving simultaneously a broadening of upstream SOL profiles and an energy load reduction at the outer divertor target.

The qualification of the density shoulder amplitude reveals a saturation whenever the QCE-phase is achieved. The saturation occurs when α_t exceeds $\sim$0.5 which is the suggested criterion being in the QCE-phase for AUG [3]. Near SOL λ_n behaves similar to the density shoulder. At the same time, the neutral pressure measured in the main chamber follows linearly α_t, whereas the divertor neutral pressure is not uniform with varying q_{95}. This observation is also covered by neutral flux measurements from manometers at similar poloidal locations.

The evolution of the energy loads on non-divertor PFCs throughout the entire scan follow linearly α_t. Radiative reconstructions implies a correlation between the radiation peak in the upper divertor with an enhancement of filamentary transport. The energy deposition on the upper divertor is mostly caused by radiation. Furthermore, the extension of the first wall energy loads to a set of AUG discharges preserves the trend in the first wall energy load scaling.

The analysis of filament properties show a clear increase of the particle flux $\Gamma_{r,fil}$ with increasing α_t. The variation is caused by an increase of the filament detection frequency as well as filament density. Both, electron and ion temperature, reveal no substantial variation whenever the QCE-phase is achieved. Leveraging on the work performed in [86] an investigation of the impact of upper triangularity in setting heat and particle convective filamentary transport will be performed, to further elaborate the connection between the separatrix turbulence level and the filament characteristics measured in the far-SOL.

Significant tungsten gross erosion values are obtained due to sputtering by impurity ions. The main source of gross erosion is the elevated background plasma more than the filaments themselves. The absolute magnitude of gross sputtering depends on the considered impurity species and the inclination of the magnetic field on the tile surface. For ITER, accurate numerical studies facing the challenge of prompt redeposition together with studies on the species mix and the wetted area are demanded in order to predict the expected lifetime of the ITER first wall.

Acknowledgments

This work has been carried out within the framework of the EUROfusion Consortium, funded by the European Union via the Euratom Research and Training Programme (Grant Agreement No 101052200 - EUROfusion). Views and opinions expressed are however those of the author(s) only and do not necessarily reflect those of the European Union or the European Commission. Neither the European Union nor the European Commission can be held responsible for them.

The authors would like to thank Ralph Dux, Michael Griener, Arne Kallenbach, Rudi Neu, Richard Pitts and Klaus Schmid for fruitful discussions.

ORCID iDs

A. Redl https://orcid.org/0000-0002-7254-3501
N. Vianello https://orcid.org/0000-0003-4401-5346
J. Adamek https://orcid.org/0000-0001-8562-1233
M. Bernert https://orcid.org/0000-0003-1131-0867
G. Birkenmeier https://orcid.org/0000-0001-7508-3646
D. Brida https://orcid.org/0000-0002-8647-7058
P. David https://orcid.org/0000-0003-4837-8507
M. Faitsch https://orcid.org/0000-0002-9809-7490
G. Grenfell https://orcid.org/0000-0003-0107-5787
V. Rohde https://orcid.org/0000-0003-4895-7664
B. Tal https://orcid.org/0009-0009-5316-6358

References

[1] Faitsch M., Eich T., Harrer G.F., Wolfrum E., Brida D., David P., Griener M. and Stroth U. (the ASDEX Upgrade Team and the EUROfusion MST1 Team) 2021 *Nucl. Mater. Energy* **26** 100890
[2] Greenwald M. 2002 *Plasma Phys. Control. Fusion* **44** R27
[3] Faitsch M., Eich T., Harrer G., Wolfrum E., Brida D., David P., Dunne M., Gil L., Labit B. and Stroth U. (the ASDEX

Upgrade Team and the EUROfusion MST1 Team) 2023 *Nucl. Fusion* **63** 076013
[4] Goldston R., Reinke M. and Schwartz J. 2017 *Plasma Phys. Control. Fusion* **59** 055015
[5] Kukushkin A., Pacher H., Pacher G., Kotov V., Pitts R. and Reiter D. 2013 *J. Nucl. Mater.* **438** S203–7
[6] Harrer G. *et al* (the EUROfusion MST1 Team and the ASDEX Upgrade Team) 2018 *Nucl. Fusion* **58** 112001
[7] Labit B. *et al* 2019 *Nucl. Fusion* **59** 086020
[8] Harrer G.F. *et al* (the ASDEX Upgrade Team and the EUROfusion MST1 Team) 2022 *Phys. Rev. Lett.* **129** 165001
[9] Wolfrum E. *et al* (the ASDEX Upgrade Team) 2011 *Plasma Phys. Control. Fusion* **53** 085026
[10] Stober J., Maraschek M., Conway G., Gruber O., Herrmann A., Sips A., Treutterer W. and Zohm H. (The ASDEX Upgrade Team) 2001 *Nucl. Fusion* **41** 1123
[11] Wagner F. *et al* 1984 *Phys. Rev. Lett.* **53** 1453
[12] Zohm H. 1996 *Plasma Phys. Control. Fusion* **38** 105
[13] Griener M. *et al* 2020 *Nucl. Mater. Energy* **25** 100854
[14] Vianello N. *et al* (the ASDEX Upgrade Team, the TCV Team, the EUROfusion MST1 Team and the JET Contributors) 2021 *paper Presented at 2020 IAEA Fusion Energy Conf. (NICE) [EX/P3-14]*
[15] Sun H., Wolfrum E., Eich T., Kurzan B., Potzel S. and Stroth U. (the ASDEX Upgrade Team) 2015 *Plasma Phys. Control. Fusion* **57** 125011
[16] Stagni A. *et al* (the TCV Team and the EUROfusion MST1 Team) 2022 *Nucl. Fusion* **62** 096031
[17] Carralero D. *et al* 2015 *J. Nucl. Mater.* **463** 53–59
[18] Février O. *et al* (the TCV Team and the EUROfusion MST1 Team) 2020 *Plasma Phys. Control. Fusion* **62** 035017
[19] Wynn A. *et al* (JET Contributors) 2018 *Nucl. Fusion* **58** 056001
[20] Sun H. *et al* 2022 *Nucl. Fusion* **63** 016021
[21] Eich T., Manz P., Goldston R., Hennequin P., David P., Faitsch M., Kurzan B., Sieglin B. and Wolfrum E. (the ASDEX Upgrade team and the EUROfusion MST1 team) 2021 *Nucl. Fusion* **61** 056016
[22] Eich T. and Manz P. (the ASDEX Upgrade team) 2020 *Nucl. Fusion* **60** 086017
[23] Scott B. 2002 *New J. Phys.* **4** 52
[24] Scott B. 2007 *Plasma Phys. Control. Fusion* **49** S25
[25] Rogers B.N., Drake J.F. and Zeiler A. 1998 *Phys. Rev. Lett.* **81** 4396
[26] Wenninger R. *et al* 2017 *Nucl. Fusion* **57** 046002
[27] Birkenmeier G. *et al* (The ASDEX UpgradeTeam) 2015 *Nucl. Fusion* **55** 033018
[28] Dux R., Loarte A., Angioni C., Coster D., Fable E. and Kallenbach A. 2017 *Nucl. Mater. Energy* **12** 28–35
[29] Redl A., Eich T., Vianello N. and David P. (the ASDEX Upgrade Team and the EUROfusion MST1 Team) 2023 *Nucl. Mater. Energy* **34** 101319
[30] Sieglin B., Faitsch M., Herrmann A., Brucker B., Eich T., Kammerloher L. and Martinov S. 2015 *Rev. Sci. Instrum.* **86** 113502
[31] Nille D., von Toussaint U., Sieglin B. and Faitsch M. 2018 *Bayesian Inference and Maximum Entropy Methods in Science and Engineering* vol 55–64 (Springer)
[32] Herrmann A., Junker W., Gunther K., Bosch S., Kaufmann M., Neuhauser J., Pautasso G., Richter T. and Schneider R. 1995 *Plasma Phys. Control. Fusion* **37** 17–29
[33] Eich T., Sieglin B., Scarabosio A., Fundamenski W., Goldston R. and Herrmann A. 2011 *Phys. Rev. Lett.* **107** 215001
[34] Loarte A. *et al* 1999 *J. Nucl. Mater.* **266–269** 587–92
[35] Redl A., Hohmann T., Eich T., Vianello N., Bernert M., David P., den Harder N., Herrmann A., Rohde V. and Weiland M. (the ASDEX Upgrade Team and the EUROfusion MST1 Team) 2023 *Plasma Phys. Control. Fusion* **65** 115003
[36] Weinlich M. and Carlson A. 1996 *Contrib. Plasma Phys.* **36 S1** 53–59
[37] Reichbauer T., Drenik A., McDermott R. and Rohde V. (the ASDEX Upgrade Team) 2019 *Fusion Eng. Des.* **149** 111325
[38] Neuwirth D., Rohde V. and Schwarz-Selinger T. (the ASDEX Upgrade Team) 2012 *Plasma Phys. Control. Fusion* **54** 085008
[39] Vorpahl C., Suttrop W., Ebner M., Streibl B. and Zohm H. (the ASDEX Upgrade Team) 2013 *Fusion Eng. Des.* **88** 537–40
[40] Haas G. and Bosch H.-S. 1998 *Vacuum* **51** 39–46
[41] Kurzan B. and Murmann H.D. 2011 *Rev. Sci. Instrum.* **82** 103501
[42] Stangeby P. 2000 *The Plasma Boundary of Magnetic Fusion Devices* (CRC Press)
[43] Willensdorfer M., Wolfrum E., Fischer R., Schweinzer J., Sertoli M., Sieglin B., Veres G. and Aumayr F. (the ASDEX Upgrade Team) 2012 *Rev. Sci. Instrum.* **83** 023501
[44] Ochoukov R., Dreval M., Bobkov V., Faugel H., Herrmann A., Kammerloher L. and Leitenstern P. (The ASDEX Upgrade Team and the EUROfusion MST1 Team) 2020 *Rev. Sci. Instrum.* **91** 063506
[45] Adamek J. *et al* 2008 *Contrib. Plasma Phys.* **48** 395–9
[46] Adamek J. *et al* 2016 *Rev. Sci. Instrum.* **87** 043510
[47] Grenfell G. *et al* 2022 *Rev. Sci. Instrum.* **93** 023507
[48] Kočan M *et al* 2012 Ion energies and currents of type I and mitigated ELMs in the ASDEX Upgrade far scrape-off layer Nucl. Fusion **52** 023016
[49] Tsui C. *et al* (the TCV Team and the EUROfusion MST1 Team) 2018 *Phys. Plasmas* **25** 072506
[50] D'Ippolito D., Myra J. and Zweben S. 2011 *Phys. Plasmas* **18** 060501
[51] Teliban I., Block D., Piel A. and Greiner F. 2007 *Plasma Phys. Control. Fusion* **49** 485
[52] Hutchinson I.H. 2002 *Plasma Phys. Control. Fusion* **44** 2603
[53] Carralero D., Artene S., Bernert M., Birkenmeier G., Faitsch M., Manz P., de Marne P., Stroth U., Wischmeier M. and Wolfrum E. (The ASDEX Upgrade Team and the EUROfusion MST1 Team) 2018 *Nucl. Fusion* **58** 096015
[54] Brunner D., LaBombard B., Ochoukov R. and Whyte D. 2013 *Rev. Sci. Instrum.* **84** 033502
[55] Dreval M., Rohraff D., Xiao C. and Hirose A. 2009 *Rev. Sci. Instrum.* **80** 103505
[56] Fonck R., Darrow D. and Jaehnig K. 1984 *Phys. Rev.* A **29** 3288
[57] Viezzer E., Pütterich T., Dux R. and McDermott R. (the ASDEX Upgrade Team) 2012 *Rev. Sci. Instrum.* **83** 103501
[58] Fischer R., Giannone L., Illerhaus J., McCarthy P. and McDermott R. (A. U. Team) 2020 *Fusion Sci. Technol.* **76** 879–93
[59] Hohmann T., Redl A., Rohde V., Schall G. and Schandrul M. (the ASDEX Upgrade Team) 2023 *Fusion Eng. Des.* **187** 113365
[60] Richter T. and Vernickel H. 1994 *Rev. Sci. Instrum.* **65** 1613
[61] Matthews G. *et al* (JET Contributors) 2017 *Nucl. Mater. Energy* **12** 227–33
[62] Butland A. and Maddison R. 1973 *J. Nucl. Mater.* **49** 45–56
[63] Dorogokupets P., Ponomarev E. and Melekhova E. 1999 *Petrology* **7** 574–91
[64] David P., Bernert M., Pütterich T., Fuchs C., Glöggler S. and Eich T. (the ASDEX Upgrade Team) 2021 *Nucl. Fusion* **61** 066025
[65] Mlynek A. *et al* (the ASDEX Upgrade Team) 2011 *Nucl. Fusion* **51** 043002
[66] Herrmann A., Eich T., Rohde V., Fuchs C.J. and Neuhauser J. (the ASDEX Upgrade Team) 2004 *Plasma Phys. Control. Fusion* **46** 971

[67] Eich T. *et al* (The ASDEX Upgrade Team and the JET EFDA Contributors) 2013 *Nucl. Fusion* **53** 093031
[68] Scott B. 1997 *Plasma Phys. Control. Fusion* **39** 1635
[69] Sieglin B., Faitsch M., Eich T., Herrmann A. and Suttrop W. (the MST1 Team and the ASDEX Upgrade Team) 2017 *Phys. Scr.* **2017** 014071
[70] Brida D. *et al* (the ASDEX Upgrade Team and the EUROfusion MST1 Team) 2017 *Nucl. Fusion* **57** 116006
[71] Brida D., Silvagni D., Eich T., Faitsch M. and McCarthy P. (the ASDEX Upgrade Team and the MST1 Team) 2020 *Plasma Phys. Control. Fusion* **62** 105014
[72] Schneider P.A. *et al* (the ASDEX Upgrade Team, the DIII-D Team and JET EFDA Contributors) 2012 *Plasma Phys. Control. Fusion* **54** 105009
[73] Vianello N. *et al* (the ASDEX Upgrade Team, the TCV Team and the EUROfusion MST1 Team) 2020 *Nucl. Fusion* **60** 016001
[74] Tsui C.K. *et al* (T. Team and M. Team) 2022 *Phys. Plasmas* **29** 062507
[75] Kocan M. *et al* (the ASDEX Upgrade Team) 2013 *Nucl. Fusion* **53** 073047
[76] Kocan M., Gennrich F., Kendl A. and Müller H. (the ASDEX Upgrade Team) 2012 *Plasma Phys. Control. Fusion* **54** 085009
[77] Pitts R. *et al* 2011 *J. Nucl. Mater.* **415** S9557–964
[78] Mancini D., Ricci P., Vianello N., Giacomin M. and Coroado A. 2021 *Nucl. Fusion* **61** 126029
[79] Yamamura Y., Itikawa Y. and Itoh N. 1983 Angular dependence of sputtering yields of monatomic solids *IPPJ-AM-26*
[80] Cohen R. and Ryutov D. 1995 *Phys. Plasmas* **2** 2011–9
[81] Stangeby P. 2012 *Nucl. Fusion* **52** 083012
[82] Bohdansky J. 1984 *Nucl. Instrum. Methods Phys. Res.* **2** 587–91
[83] Schmid K., Mayer M., Adelhelm C., Balden M. and Lindig S. (the ASDEX Upgrade team) 2010 *Nucl. Fusion* **50** 105004
[84] Eckstein W., Garciá-Rosales C., Roth J. and Ottenberger W. 1993 *IPP Report IPP* 9/82
[85] Tolias P. 2014 *Plasma Phys. Control. Fusion* **56** 123002
[86] Stagni A. *et al* (the TCV Team) 2024 *Nucl. Fusion* **64** 026016